Effects of Microstructure on the Electrical Properties of Amorphous Solid Water

Caixia Bu
Guigang, Guangxi, China

M.A., University of Virginia, May 2011
B.S., University of Science and Technology of China, May 2007

A Dissertation presented to the Graduate Faculty
of the University of Virginia in Candidacy for the Degree of
Doctor of Philosophy

Department of Physics

University of Virginia
December, 2014 Degree **will be Conferred**

Table of Contents

Acknowledgements

First I would like to thank all the people I have had the privilege to work with in the last four years in LASP. Foremost, I would like to thank my advisor, Raul Baragiola, for the guidance and support he provided me through years of my graduate studies and research. His keen interest towards the setbacks and progresses in my work, his mentoring and critique and his accessibility is deeply appreciated. I am also grateful to Cathy Dukes who patiently taught me the ways of the lab in the beginning years of my graduate studies, encouraged me while I was down, and offered suggestions when I was confused. I could not ask for better colleagues than Dabney Carson, Daniele Fulvio, Emma Mitchell, Ujjwal Raut, Micah Schaible, Jianming Shi and Adam Woodson. I am indebted to you all for the help you provided within and beyond the laboratory. Working closely with you all definitely made my experience more enjoyable.

I would like to thank my parents for their love and supports, and my life could have been totally different without the education they gave. My parents always had my education as their top priority and never compromised on that stance even when circumstances were dire. To them, I dedicated this piece of work. I would like to thank my siblings. They patiently listened while I grumbled away and constantly encouraged me while I was down. They took care of our parents while I studied abroad these years. Without their support, I could not have concentrated on this work; without their love, I could not have been able to keep my smiles.

I have been blessed with wonderful friends throughout my life and I must say thanks to you all. I would like to say big thanks especially to Sha Li, Shun Zheng, Siyuan Ge, and Qian Xian. The conversations, movies, hiking and tennis were wonderful stress relievers that helped me maintain my sanity. The meals you provided during me tough experiment periods beat the best restaurant in the world.

I would like to thank peoples in the Department of Physics. I would like to thank Professor Bob Jones, Olivier Pfister, Bellave Shivaram and Nilanga Liyanage, for their constant support on my research. I would like to thank Helen McLaughlin, Dawn Shiffflett, and Tammie Shifflett. I appreciated you all helped to take care of my financial, academic and visa issues. Without your help, this work would not happen. I would like to thank Gwen Dellinger. The coffee you made gave me a good start of my every day.

Lists of Symbols and Abbreviations

Å	Angstrom
A	area
ASW	amorphous solid water
CPD	contact potential difference
d, L	film thickness
DB	dangling bond
ε	dielectric constant / relative permittivity
ε_o	permittivity free space
E	ion energy
eV	electron volts
f	frequency
Δf	frequency shift
$\emptyset, P,$	porosity
K	Kelvin
m	mass
M	molecular mass
ML	monolayer, 1 ML = 1×10^{15} molecules/cm2
µm	micron
n	number of monolayer
nm	nanometer
QCM	quartz crystal microbalance
QMS	quadrupole mass spectrometer

q, Q	charge
ρ	density
ρ_c	compact ice density
s	microbalance constant / Sauerbery's constant
$S, dE/dx$	stopping power
T	temperature
Torr	pressure unit
TPD	temperature programmed desorption
TRIM	Transport and Range of Ions in Matter
τ	time constant
UHV	ultrahigh vacuum
UV	ultraviolet-visible
V_s	surface potential
WF	work function
z	atomic number

List of Figures

Chapter One

Introduction

Water ice has been studied extensively in recent years due to its abundance in astronomical environments [1, 2]. It is well established that water ice condensed from water vapor onto cold substrates (< ~130 K, also called amorphous solid water (ASW)) has properties greatly different from those of its crystalline counterparts. A crucial characteristic of ASW films is their microporosity, which directly affects other important properties. A significant finding of this thesis is the importance of microporosity on electrical properties of ASW at low temperatures, with emphasis on the spontaneous polarization and motion of ions in the ASW.

1. Properties of ASW Films

1.1. Porosity of ASW

Gas adsorption experiments have revealed that ASW has micropores (defined as pore width < 2 nm) presenting an effective adsorption area as large as hundreds of m^2/g [3, 4, 5, 6, 7]. Distribution of the binding energy for gas adsorption in the micropores can be estimated by fitting the gas adsorption isotherms with the empirical equations [7]. However, when pores are not connected to the external surface of the ASW, such gas adsorption experiments are ineffective. Infrared absorption spectra show enhanced features in the region of the dangling OH bands (~2.7 μm) of ASW, assigned to abundant doubly-coordinated and triply-coordinated water molecules on surfaces of the pores in

ASW [8, 9]. The integrated absorption of these bands, which are usually insignificant in compact ice, is indicative of the total pore surface area in the ASW. The average density (ρ) of an ASW film can be calculated with a combination of the thickness obtained with UV-Visible interferometry [10, 11] and the areal mass measured with quartz crystal microgravimetry [12]. The average porosity of the ASW is defined as $\emptyset = 1 - \rho/\rho_c$, where ρ_c is the density of the compact ice.

The porosity of ASW decreases with increasing deposition temperature [13] and increases with increasing incident angle of the vapor beam [5, 6]. The fact that limited microporosity results during growth even at relatively high temperatures close to the crystallization transition (~150 K) suggests that diffusion during deposition is negligible [2, 13].

It has been confirmed with multiple techniques that warming ASW to temperatures higher than the growth temperature, but below the onset for crystallization, produces irreversible exothermic changes, making the ASW more compact by closing pores. Observations include decrease of gas adsorption ability [3, 4, 7, 14], diminishing intensity of the dangling OH features in the infrared absorption spectra [9], reduced film thickness [7, 11] and changes in parameters of positron annihilation spectra [15]. For instance, Bar-Nun et al. [4] found that the gas absorption area decreased by ~90% when the ASW film was heated from 10 – 20 K to 122 K; Rowland et al. [9] showed that the intensity of the dangling OH features diminished if the ASW film was heated from 15 K to 60 K and disappeared if heated to 120 K; and the thickness of a porous ice film deposited at 40 K reduced from ~540 nm to ~376 nm if the film was heated from 40 K to ~140 K [7].

Remarkably, Raut et al. [7] revealed some mesopores (defined as pore width ~2 – 50 nm) formed when films were deposited at large incident angles, in addition to having micropores, and some of the mesopores were retained upon warming to ~140 K. The micropores also disappear if the ASW is under ion irradiation [16]. However, the collapsing processes are not well understood.

Buch [17] proposed that the reason ASW is microporous is that incoming molecules attach preferentially to dangling bonds sticking out of the surface and thus stick out even more, forming increasingly longer surface protrusions. As the incident angle of the vapor beam increases, ballistic deposition simulations [6, 18], simpler "hit and stick" models, suggest that filamentary pores form on the incident plane with a tilting angle that is close but smaller than the incident angle of the vapor beam, as shown in Figure 1.1. The filamentary structure of the pore networks in ASW has not been confirmed in the laboratory yet.

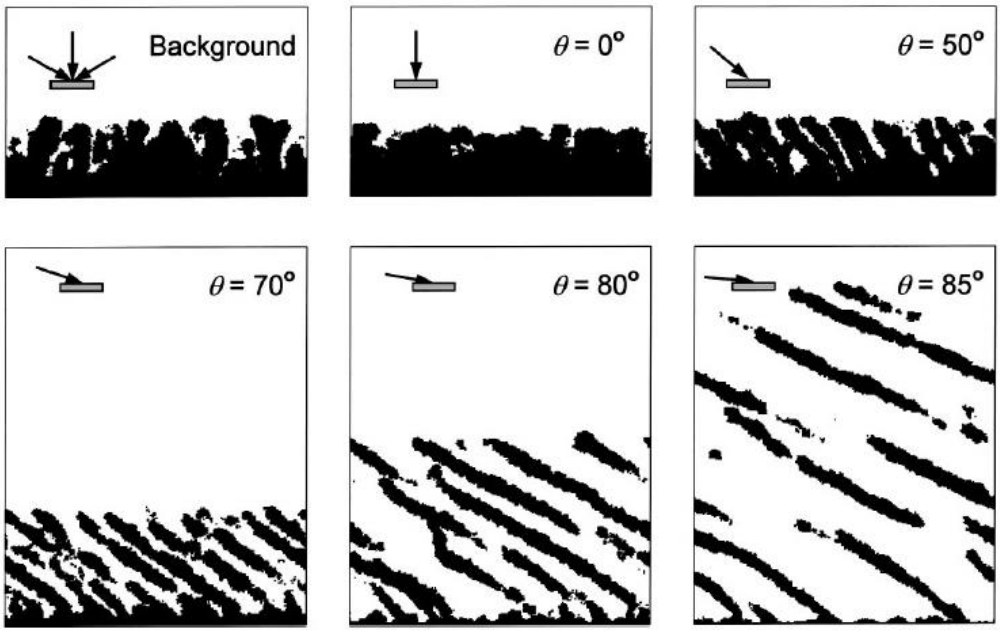

Figure 1.1 Filamentary pores. Two-dimensional sections through the 50 ML (1 ML = 1.05×10^{15} molecules/cm^2) films obtained from the three-dimensional ballistic deposition simulation in Ref. 6. The apparent presence of the unattached parts of the filaments is a result of presentation of two-dimensional sections from three-dimensional simulations.

1.2. Polarization of ASW

Water molecules have molecular dipoles of several Debye (1 D = 3.34 $\times 10^{-30}$ C. m). In normal high-temperature ice (> ~150 K) there is a balance of "up" and "down" dipoles resulting in no net polarization. However, it has been seen that water ice formed by vapor deposition on cold substrates (< ~140 K) becomes spontaneously polarized via partial alignment of the water molecules. Evidences include induced currents on the metal substrates during condensation of the water ice films [19, 20], enhanced OH stretch features in the vibrational spectra of ice films obtained with the optical sum-frequency vibrational spectroscopy [21] and large voltages across the ice films, as measured by Kelvin probes [22]. The spontaneous polarization of the water ice during condensation doesn't depend on the substrate potential with respect to the chamber walls or the substrate material [19, 20] but strongly depends on substrate temperature. However, the mechanism inducing the polar ordering of the water molecules is controversial in the literature. Some authors [19, 20, 22] suggested the polarization results from the asymmetry at the interfaces of the film and the substrate while others [21] suggested water molecules are oriented by the asymmetry of the solid-vacuum interface. The consensus view is that depolarization happens when ice films are heated, but the mechanism involved is poorly understood, considering the limited diffusion of molecules at low temperatures.

1.3. Ion Motion in Water Ice

The experimental results about the motion of ions in water ice at low temperatures vary widely and the mechanism involved is poorly understood. The degree of proton mobility in crystalline ice is very high (~10^{-9} – 10^{-7} $m^2V^{-1}s^{-1}$, depending on temperature), theoretically expected from the Grotthuss mechanism [23] in which the effective motion of a proton involves a sequence of proton tunnelings along the hydrogen-bonded chain of water molecules. Experimental studies have indicated the proton transport in ice is a thermally activated process that occurs extremely slowly at temperatures below 120 K [24]. Cowin et al. [25, 26] even concludes that ions do not move at all in ice at temperatures below 190 K measuring charging by soft-landing (eV) ions deposited on top of the ice films. Kang et al. [27, 28, 29] comprehensively investigated motions of hydronium and hydroxide ions in ice films at low temperatures (< ~140 K) and derived the conclusion that protons are significantly mobile in water ice above ~130 K with the preference to reside at the ice surface rather than in the interior. Previous studies in our lab [30, 31] on electrostatic charging/discharging of ice films with the impact of 1 – 200 keV Ar^+ ions at 15 – 160 K suggested that the trapped charges leak to the substrate at a rate increasing with temperature.

1.4. Cracks in ASW

Cracks, wide boundaries between particles, have been seen during growth of ASW at low temperatures in several studies [32, 33, 34, 35]. There is a critical film thickness for cracking that increases with growth temperature [34] and with angle of incidence of the water molecules [35]. Cracks may also form if a thin ASW film is heated above ~150 K due to thermal stresses and density variations during phase transformations [11]. The

formation of cracks likely causes abrupt increase in optical reflectance [36, 37] and in gas desorption [38]. In this thesis, we observed the effects of cracks on spontaneous polarization and motion of ions in ASW.

1.5. Astrophysical Relevance

Interstellar ASW, exposed to UV photons, solar wind, cosmic rays and energetic charged particles trapped by the planetary magnetosphere, will be charged or partially charged, resulting from trapping of charges implanted by the projectiles or from the emission of secondary electrons/ions. The charging of the icy objects generates surface electrical fields in the icy objects, and these surface electric fields may deflect (attract) magnetospheric particles with the same (opposite) polarity from reaching the surface of the icy objects. In this thesis, we studied surface potentials of ASW resulting from spontaneous polarization or electrostatic charging/discharging, as well as evolution of the surface potentials with annealing temperature. The work in this thesis will help to understand better ice structure, ice-charge interactions and other charge related processes in the Outer Solar System and interstellar medium. Although the research in a laboratory environment lacks the complexity of processes in space, effects of microstructure/temperature on electrostatic charging/discharging presented in this thesis provide more relevance to modelers to refine their parameters when modeling the icy surfaces in space.

2. **Organization of The Thesis**

The theme of the research presented in this thesis is to investigate how the microporosity/cracking affects the spontaneous polarization and motion of ions in ASW at low temperatures. The micropores and cracks were not considered in the earlier studies on the electrical properties of the ASW and results in this thesis will be helpful in modeling/interpreting physical and chemical processes in the ASW at low temperatures.

In Chapter 2, we introduce the experimental setup and methods for this thesis. We present effects on microstructure on spontaneous polarization of ASW in the first section of Chapter 3. We studied the spontaneous polarization of ASW deposited at 10 – 110 K by measuring surface potentials of the ASW films with a Kelvin probe, focusing on dependences of the dielectric polarization on deposition temperature, film thickness, porosity and annealing temperature. We found that the polarization strongly depends on the porosity of the ASW films. A model, connecting the polarization of the ASW with the pore networks in the ASW, is proposed to explain the observations. In the second section of Chapter 3, our investigations show that the motion of ions with annealing temperature corresponded to the thermally induced evolution of the pore networks in the ASW. Effects of cracks on the polarization and motion of ions motion in ASW are presented in Chapter 4. We prepared the cracking films either by directly depositing the films with thicknesses above the critical thicknesses or by heating the films deposited on top of xenon (Xe) layers. Surface potentials of the cracking films suggested depolarization during cracking. If the cracking films were heated, the cracks/grain boundaries hindered the depolarization or ion motion. Chapter 5 summarizes the key findings and conclusions.

Reference

[1] R. E. Johnson, T. I. Quickenden, *J. Geophys. Res. E* **102**, 10985 (1997)

[2] R. A. Baragiola, *Planet Space Sci.* **51**, 953 (2003)

[3] E. Mayer and R. Pletzer, *Nature* (London) **319**, 298 (1986)

[4] A. Bar-Nun, and T. Owen, *Solar System Ices*, eds. B. Schmitt, C. De. Bergh, M. Festou (Dordrecht: Kluwer), **353** (1998)

[5] K.P. Stevenson, Greg A. Kimmel, Z. Dohnalek, R. Scott Smith, and Bruce D. Kay, *Science* **283**,1505 (1999)

[6] Z. Dohnalek, G. A. Kimmel, P. Ayotte, R. S. Smith, and B. D. Kay, *J. Chem. Phys.* **118**, 364 – 372 (2003)

[7] U. Raut, M. Fama, B. D. Teolis, and R. A. Baragiola, *J. Chem. Phys.* **127**, 204713 (2007).

[8] V. Buch and J. P. Devlin, *J. Chem. Phys.* **94**, 40091 (1991)

[9] B. Rowland and J. P. Devlin, *J. Chem. Phys.* **94**, 812 (1991)

[10] O. S. Heavens, *Optical Properties of Thin Solid Films* (Dover, New York, 1991)

[11] M. S. Westley, G. A. Baratta and R. A. Baragiola, *J. Chem. Phys*. **108**, 8 (1998)

[12] M. A. Allodi et al., *Space Sci. Rev*. **180**, 101 (2013)

[13] D. E. Brown and S. M. George, C. Huang, E. K. L. Wong, Keith B. Rider, R. S. Smith, and B. D. Kay, *J. Phys. Chem.* **100**, 4988-4995 (1996)

[14] J. A. Ghormley, *J. Chem. Phys.* **46**, 1321 (1967)

[15] Y. C. Wu, J. Jiang, A. Kallis, S. J. Wang, and P. G. Coleman, *Phys. Rev. Lett.* 105, 066103 (2010)

[16] U. Raut, M. Fama, B. D. Teolis, and R. A. Baragiola, *J. Chem. Phys.* **127**, 244511 (2007)

[17] V. Buch, *J. Chem. Phys.* **96,** 3814 (1992)

[18] A. G. Dirks and H. J. Leamy, *Thin solid films* **47**, 219-233 (1977)

[19] K. Kutzner, *Thin Solid Films* **14**, 49 (1972)

[20] L. Onsager, D. L. Staebler, S. J. Mascarenhas, *J. Chem. Phys*. **68**, 3823 (1978)

[21] X. Su, L. Lianos, R. Y. Shen, and G. A. Somorjai, *Phys. Rev. Lett*. **80**, 1533 (1998)

[22] M.J. Iedema, M.J. Dresser, D. L. Doering, J. B. Rowland, W.P. Hess, A. A. Teskouras, and J. P. Cowin, *J. Phys. Chem. B* **102**, 9203 (1998)

[23] P. V. Hobbs, *Ice Physics* (Clarendon, Oxford, 1974)

[24] P. J. Wooldridge and J. P. Devlin, *J. Chem. Phys.* **88**, 3086 (1988)

[25] J. P. Cowin, A. A. Tsekouras, M. J. Iedema, K. Wu and G. B. Ellison, *Nature* **398**, 405 (1999)

[26] A. A. Tsekouras, M. J. Iedema, and J. P. Cowin, *Phys. Rev. Lett.* **80**, 26 (1998)

[27] C. W. Lee, P. R. Lee, Y. K. Kim and H. Kang, *J. Chem. Phys.* **127**, 084701 (2007)

[28] E-S. Moon, C-W. Lee and H. Kang, *Phys. Chem. Chem.Phys.* **10**, 4814 (2008).

[29] S-C. Park, E-S. Moon and H. Kang, Phys. Chem. Chem. Phys. **12**, 12000 (2010)

[30] J. Shi, M. Fama, B. D. Teolis, R.A. Baragiola, *Nuclear Instrument and methods in physics research B* **268**, 2888-2891 (2010)

[31] J. Shi, M. Fama, B.D. Teolis, R. A. Baragiola, *Phys. Rev. B* **85**, 035424 (2012)

[32] B. E. Wood, J. A.Roux, *J. Opt. Soc. Am* **72**, 720 – 728 (1982)

[33] B. Schmitt, J. Ocampo, J. Klinger, *J. Phys.* (Paris) **48**, CI, 519 – 525 (1987)

[34] D. A. Bahr, Ph. D. Thesis, University of Virginia 2000

[35] D. Pugh, M. Sc Theis, University of Virginia 2002

[36] A. S. Drobyshev, N. V. Atapina, D. N. Garipogly, S. L. Maksimov, and E. A. Sampshkin, *Low Temp. Phys.* **19**, 404 (1993)

[37] A. S. Drobyshev, *Low Temp. Phys.* **22**, 123 (1996)

[38] R. S. Smith, C. Huang, E. K. L. Wong, and B. D. Kay, *Surf. Sic.* **367**, 13 – 18 (1996)

Chapter Two

Experimental Details

2.1 Ice Chamber

Experiments were conducted in an oil-free ultra-high vacuum (UHV) chamber (Figure 2.1) with a base pressure of ~ 2×10^{-10} Torr. The base pressure was achieved by sequential pumping of the chamber by turbo pump (Pfeiffer, TMU065) backed with a scroll pump (Varian, SH-100) and by a cryogenic pump (CTI, Cryo-Torr 8). The system was equipped with a Kelvin probe (Section 2.3.1), a quadrupole mass spectrometer (QMS) (Section 2.3.2), a low energy ion gun (Section 2.3.3), a microcapillary-array doser (Section 2.2.4), a UV-Visible spectrometer (Section 2.3.4) and a long-distance microscope coupled with a digital camera (Section 2.3.5). The target assembly (Section 2.2.1) was mounted on a rotatable flange, and could be positioned to face any of the instruments above. An open-cycle refrigerator (APD Cryogenics) was used to cool the target assembly with liquid helium (Section 2.2.3), allowing the sample holder to reach a temperature as low as 7 K.

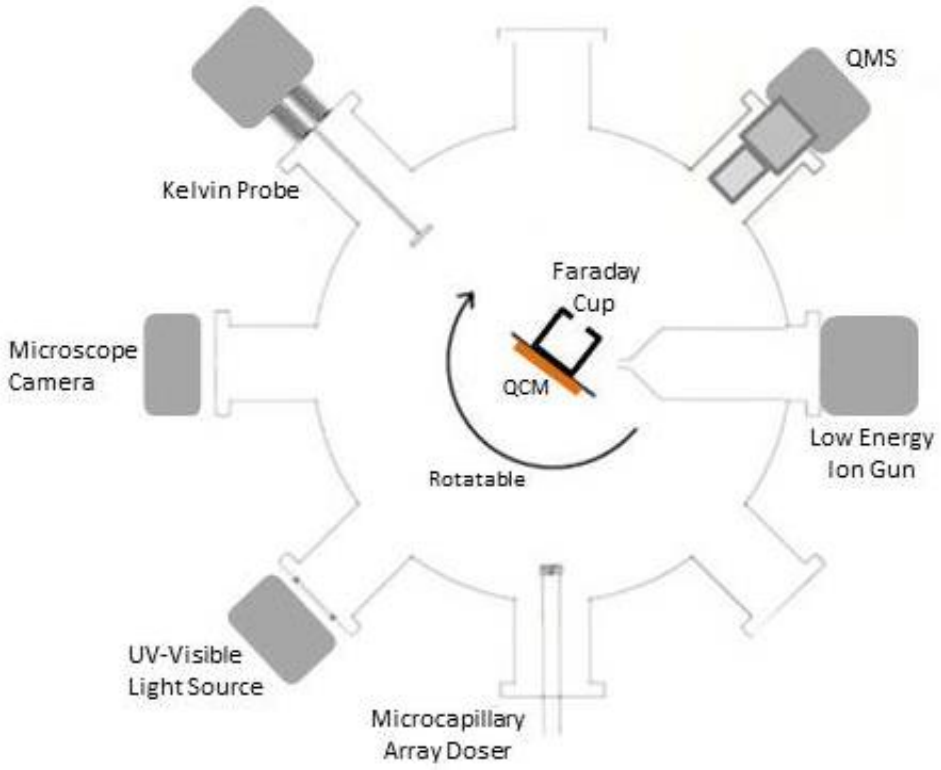

Figure 2.1 Schematic drawing of the ice chamber. Films are grown by cooling the QCM with a liquid helium cryostat and exposing the front face of the QCM to the doser. Films of varying porosity can be grown by adjusting the angle of incidence between sample normal and molecular vapor / gas beam. Ion beam current is measured with a Faraday cup mounted behind the QCM.

2.2 Target System and Sample Deposition

2.2.1 Target Assembly

The target assembly (Figure 2.2) consists of a quartz crystal microbalance (QCM), a silicon diode temperature sensor, a resistive heater (50 Ohms, 50 W), and a Faraday cup. All pieces are mounted on a copper block cooled by the open-cycle refrigeration. We used indium at the interfaces of the pieces (except the Faraday cup) to ensure good thermal contact. The target temperature, as well as the frequency of the QCM, was recorded by a LabView program.

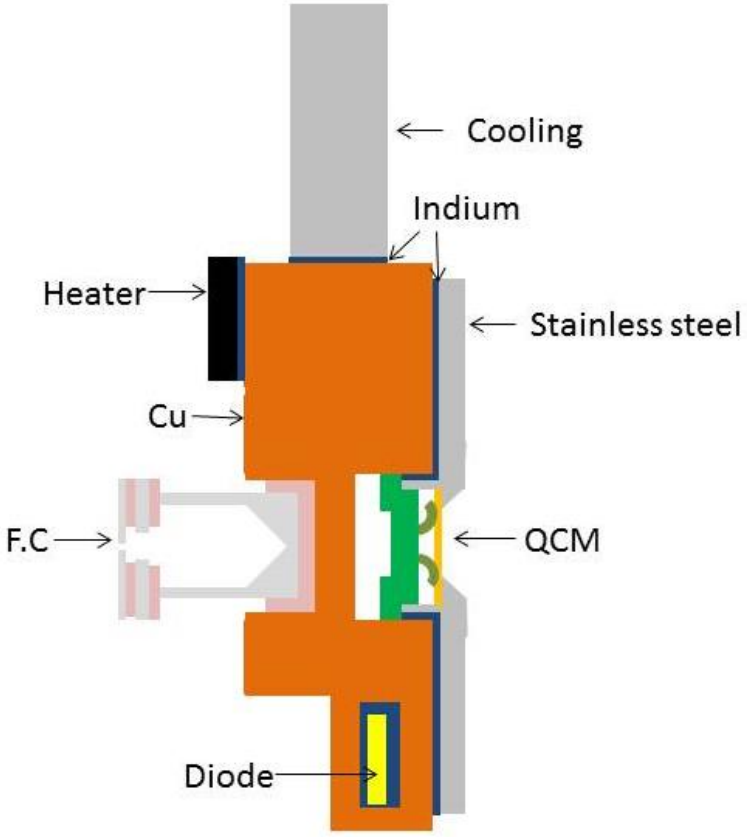

Figure 2.2 Schematic drawing of the target assembly

2.2.2 Quartz Crystal Microbalance

Films were deposited by vapor condensation onto the QCM, which had a sensitive area of 0.28 cm^2 and was coated with a 100-nm gold layer. The use of QCM to study thin film growth, sublimation and desorption is very popular in scientific research and industry due to the QCM's high accuracy, sensitivity, small size and compatibility with ultra-high vacuum [1]. Making use of the piezoelectric effect intrinsic to quartz crystals, the QCM is driven to oscillate mechanically by an applied alternating voltage with a frequency close to the QCM's resonant frequency. The QCM used here had a

where M is the molecular mass. The conversion factor μ is 0.4015 s for H_2O, 0.0564 s for Xe and 0.4618 s for methane. If the film density (ρ) is known, the thickness of the film (d) can be calculated from the change in the frequency (Δf) by

$$d = -S \cdot \frac{\Delta f}{\rho} \tag{2.3}$$

The resonant frequency of the crystal also depends on temperature; therefore, a careful control of temperature is essential [1]. Within the temperature range of 10 – 140 K, the typical experimental temperature range for ice studies, a variation of 1 K can cause a shift in frequency of 10 – 50 Hz, depending on the temperature within this range. To measure the change of the areal mass upon heating in the temperature programmed desorption (TPD) experiments, the frequency of the bare QCM heated at the same rate was used as a reference to correct for the temperature-induced change in the frequency, allowing detection of change in frequency solely due to the sample mass with an accuracy of 0.1 ML.

The resonant frequency of the QCM also depends on stress [1] which is caused by internal stresses during the growth of films of thickness of the order of microns or by a temperature gradient when a projectile beam impinges on the crystal. An abrupt release of stress can cause a sharp change in the frequency, which can serve as an indicator of the appearance of cracks in the experiments studying the fracture of the ice films. However, with a cracked ice film on top, the frequency of the QCM upon heating may not respond to the temperature in the same way as that of the bare QCM, and other techniques, e.g. mass spectrometry, were used to detect the sample desorption.

2.2.3 Target Temperature Control

The target was cooled by an open-cycle cooling system with liquid helium capable of cooling the target assembly down to 7 K. The open-cycle cooling system allows a fast cooling/heating rate (~ 5 K/minute) and a stable vibration-free environment, critical for measurements of contact potential difference with a Kelvin probe, as discussed later. This open-cycle cooling, coupled with resistive heating, allows us to control the temperature to fluctuate within ~ ±0.2 K of the intended temperature in the temperature range of 10 – 220 K. This degree of temperature stability results in a mass-independent fluctuation of the QCM frequency of ~ 1 – 10 Hz. Further details about the cooling system are available in Shi's thesis [2].

The target temperature was measured with a silicon diode temperature sensor (Scientific Instruments, Si-410C) mounted into the copper block. The sensor has an accuracy of ±0.5 K for T < 25 K and ± 1 K for T > 25 K. The voltage drop across the diode under a constant current of 10 μA was monitored with a temperature controller (Lakeshore 330) and converted to the output temperature with a 0.01 K resolution by the built-in function in the temperature controller. Calibration of the silicon diode was accomplished by immersing it in liquid nitrogen at atmospheric pressure; it read 77.4 K, close to expected 77.2 K. A power resistive heater (Caddock Model – MP9100, 50 Ω, 50 W) was mounted on the copper block to heat the target assembly. The output power of the heater was provided by the temperature controller. The cooling of the target was controlled by the flow rate of the liquid helium with setting parameters listed in Shi's thesis as references [2]. Once the liquid helium flow rate was set, the temperature

controller measured the target temperature and adjusted the output power of the heater with a built-in negative-feedback control algorithm to maintain the intended target temperature or heating /cooling rate. Stable target temperatures within 10 – 220 K were achieved and the heating/cooling rate was set at 2 K/minute or 5 K/minute in most of the experiments.

2.2.4 Sample Deposition

Films were deposited on the cold QCM from high-purity vapor/gas passed through a collimating micro-capillary array doser, and the areal masses were derived from the resulting change in the QCM frequency as discussed in Section 2.3.2. The doser is a 500-μm thick, 13 mm diam. glass dish that has 6-μm holes spaced 10 μm apart (Figure 2.3). The capillary doser provides a collimated beam of the gas molecules, and makes it feasible to deposit films with uniform thickness across the sensitive area of the QCM. The doser was mounted on a custom-manufactured linear translator and positioned ~ 1 inch away from the QCM during deposition, but not closer in order to reduce the radiative heat transfer onto the sample. The films were deposited with the QCM facing the doser for most cases including depositions of Xe or methane films. In the experiments studying the porosity effects on the electrical and structural properties of ice films, the relative angle between the normal of the QCM and the doser was varied from 0° to 70° with a resolution of ~±1° [3].

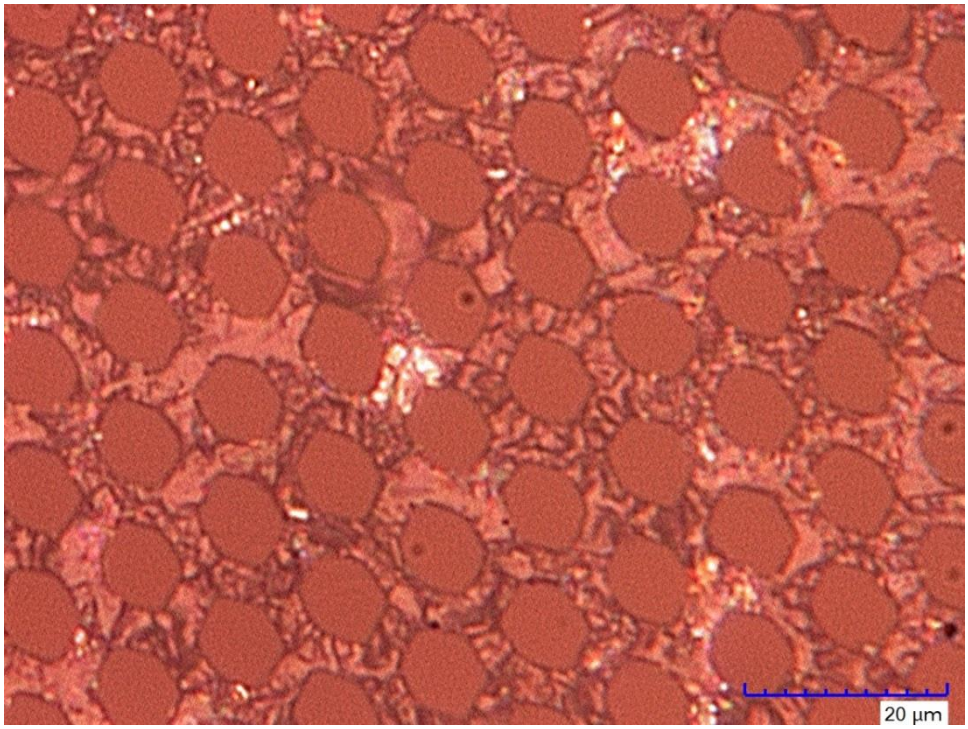

Figure 2.3 Optical microscopy image of the capillary array of the doser

The water used was high performance liquid chromatography (HPLC) grade, and gases (Xe / methane) used had a purity of 99.999%. The glass ampoule containing the water and the lecture bottles containing the research gases were attached to a continuously-baked stainless steel manifold which was pumped with a scroll pump (Varian, SH100). The HPLC-grade water in the ampoule was degassed by vacuum pumping to remove dissolved gases. The manifold was evacuated to 20 ± 5 mTorr, measured with a capacitance manometer (MKS Baratron model 222B) prior to deposition. During deposition, the manifold was filled with the water vapor or research gas to a pressure of ~10 Torr. The rate of the vapor/gas into the chamber was controlled

using a leak valve (Granville-Phillip). The growth rates were (0.5 – 1) $Hz \cdot s^{-1}$ for water films, (4 – 7) $Hz \cdot s^{-1}$for Xe and (0.2 – 0.8) $Hz \cdot s^{-1}$ or methane, corresponding to deposition fluxes of (0.2 – 0.4)×10^{15} H_2O $cm^{-2} \cdot s^{-1}$, (0.2 – 0.4)×10^{15} Xe $cm^{-2} \cdot s^{-1}$ and (0.1 – 0.4)×10^{15} CH_4 $cm^{-2} \cdot s^{-1}$ respectively.

2.3 Laboratory Instruments and Techniques

2.3.1 Kevin Probe

A Kelvin probe is a non-contact, non-destructive vibrating capacitor device used to measure the work function (WF) of conducting materials or the surface potential (V_s) of semiconductor or insulating surfaces. The WF is defined as the minimum energy needed to remove an electron from the surface (typically the topmost 1 – 3 layers of atoms or molecules) of the conducting material to a point in the vacuum immediately outside the material with zero kinetic energy. The work function is an extremely sensitive indicator of surface conditions. The traditional Kelvin probe system consists of a flat circular electrode (the tip of the Kelvin probe) suspended above and parallel to a stationary electrode (the sample), forming a simple capacitor. When the probe (tip) vibrates above the sample, a varying capacitance is produced (Figure 2.4a), represented as:

$$C_K(t) = \varepsilon_o \varepsilon_r \, A/d(t) \tag{2.4}$$

where $C_K(t)$ is the time-varying Kelvin capacitance, ε_o is the permittivity of the free space, ε_r is the relative permittivity ($\varepsilon_r = 1$ in vacuum), A is the surface area of the capacitor plane and $d(t)$ is the time-dependent plate separation. If we assume the

motion of the tip can be represented by a periodic sinusoidal vibration with the amplitude of d_1, the time-dependent separation is $d(t) = d_o + d_1 \cdot sin(\omega t)$, where $d_o$is the mean distance between the tip and the sample. The $C_K(t)$ can be rewritten as

$$C_K(t) = C_o/(1 + r\sin(\omega t)) \tag{2.5}$$

where $C_o(t) = \varepsilon_o \varepsilon_r A/d_o$ represents the mean capacity and $r = d_o/d_1$ is the modulation index. Therefore, the instantaneous total surface charge on the tip of the Kelvin probe is $Q_s = (V_c + V_b)C_K$, and the output current is $I_K(t) = (V_c + V_b)\delta/\delta t\ C_K$, where V_c represents the voltage difference between the probe tip and sample, V_b is the external voltage used to balance (or null) the circuit.

The Kelvin probe we used (Figure 2.4b) is a commercial device from KP Technology Ltd (Model UHV KP 4.5), and the main feature of this system is the off-null signal detection. The peak-to-peak output voltage (V_{ptp}) at the output of the variable gain voltage amplifier in the detection circuit is

$$V_{ptp} = (V_c + V_b)\ R_f\ G\ C_o\ \omega\ r\ sin(\omega t + \varphi) \tag{2.6}$$

where V_c represents the voltage difference between the probe tip and sample, V_b is the external voltage used to balance (or null) the circuit, R_f is the I/V converter feedback resistance, G is the gain of the preamplifier, ω is the angular frequency of vibration, and φ is a phase angle. In the traditional detection model, the WF between the two electrodes (V_c) is determined by adjusting the V_b until a zero (null) output is achieved. In the off-null detection mode, V_b is set to a range of values, and the corresponding V_{ptp}

data set will form a straight line intersecting the V_b axis at the point where $(V_c + V_b) = 0$, indicated in Eq. (2.6). The WF (V_c) is determined from this intersecting point ($V_c = -V_b$). In a normal operation, two V_b values (V_b and $-V_b$) are sufficient to produce good quality WF data in the 1 – 3 meV sensitivity range.

Figure 2.4 (a) Schematic diagram of the tip-sample spacing during the tip oscillation. The mean spacing is $d_{o,}$ and the amplitude of the tip motion is d_1, suggesting a total tip displacement of $2d_1$. (b) Kelvin probe (KP Technology Ltd, Model UHV KP 4.5)

Surface potentials of the films were deduced from measurements of the contact potential difference (CPD) with the Kelvin probe. We measured the CPD between the tip and the QCM before (CPD_1) and after (CPD_2) deposition of the film and the surface potential (V_s) of the film was $V_s = -\Delta CPD = -(CPD_2 - CPD_1)$. The same techniques were used to derive the surface potential induced by ion irradiation. The Kelvin probe provided CPD measurements with a sensitivity of ~3 mV. However, since the sample

was rotated to face the doser or the ion gun in the subsequent CPD measurements, the derived V_s typically had an error of ±2%.

2.3.2 Quadrupole Mass Spectrometer

Residual gases in the chamber were routinely checked by a quadrupole mass spectrometer (QMS) (Stanford Research Systems, RGA100). The QMS was also used to ensure purity of the research gases and to monitor desorption of the gases in the TPD experiments. The QMS ionized the gas molecules (positive ions) by energetic electrons within the ionizer, and then directed the ions towards the quadrupole mass filter, where they were separated based on their mass-to-charge ratios (M/Q, in the unit of amu). The M/Q range of the QMS was 1 – 100 amu. The QMS cannot distinguish ions having the same M/Q. A built-in Faraday cup was used to collect the ion current at high partial pressures (10^{-4} – 10^{-6} Torr), while a particle multiplier was used at low partial pressures (10^{-6} – 10^{-11} Torr). During the experiments, water signal was monitored at M/Q = 18 (H_2O^+ ions), Xe at M/Q = 66 (Xe^{++} ions) and methane at M/Q= 16 (CH_4^+ ions). The QMS was not calibrated for measurements of absolute partial pressures of the components of a gas mixture; the QMS signals only gave the relative pressures of species. The absolute total pressure of the chamber was measured with a nude ionization gauge.

2.3.3 Low Energy Ion Gun

Ion sources used were provided by a low energy ion gun (Nonsequitur Technologies, Model 1401, as shown in Figure 2.5) which has an electron impact

ionization source and provides ions with energies below 5 keV. The maximum ion beam current density was as high as $10^{17}\ ions \cdot cm^{-2} \cdot s^{-1}$ over an irradiation area of 50 μm. The source gases (H_2, He, Ne, Ar, Kr, and Xe) were fed through a leak valve into the ion source region, where accelerated electrons, emitted from the hot filament, made ionization collisions with the source gases to produce the ions. We mounted the ion gun on a linear translator (MDC, LMT 156), allowing a travel distance of 150 mm along the gun axis. The ion gun region was differentially pumped with an ion pump (Perkin-Elmer, 30 L/s) to maintain the base pressure in the main chamber. During introduction of the source gases for irradiation, the ion gun was differentially pumped by two additional turbo pumps (Pfeiffer, TMU 071P / TPU 060) in series to keep the pressure of the main chamber below 1×10^{-9} Torr. The source gas was high purity (99.999%) He for most of the experiments; high-purity Xe and Ar were used occasionally. The ion beam was defocused to a spot size of ~5 mm, and the raster size was set to ~10 mm × 10 mm. The beam spot was centered at the sensitive area of the QCM; the beam spot covered ~ 70% (200%) of the sensitive area with the raster off (on). We kept the raster on during irradiation to obtain a uniform distribution of ions across the film surface and to reduce the ion impact damage. The beam current density was measured by a Faraday cup with an aperture of ~1mm (Figure 2.2) and was controlled at $\sim1\times10^{10}\ ions \cdot cm^{-2} \cdot s^{-1}$. The aperture plane of the Faraday cup was 28 mm closer to the ion gun than the sample plane (the QCM); the measured flux dropped to nearly a third when retracting the ion gun 28 mm away from the Faraday cup. Therefore, we adjusted the current density on the sample to be (32 ± 5) % of that

measured by the Faraday cup. The irradiation time was 270 seconds for most of the experiments (a fluence of $(0.9\pm0.1)\times10^{12} ions\cdot cm^{-2}$ on the sample surface). Every time the ion gun was physically moved, we checked the alignment of the ion gun with the fluorescence emissions from a thick Ar film deposited at 20 K. Misalignment or incorrect settings of the operation parameters could be easily noticed from the much lower current density measured by the Faraday cup.

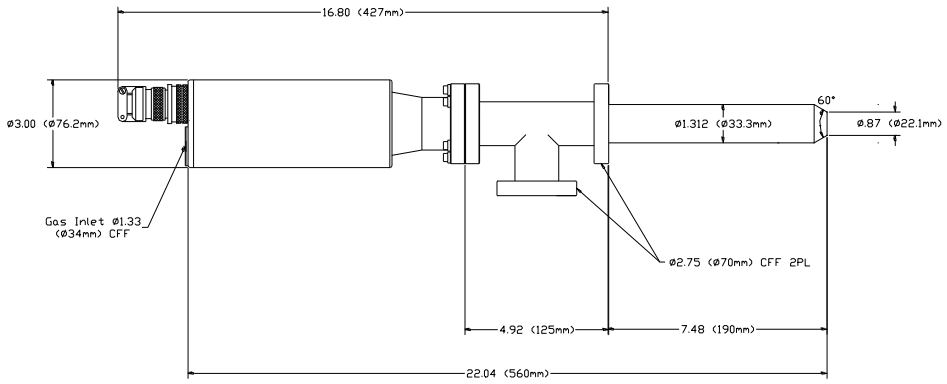

Figure 2.5 Configuration of the Nonsequitur Technologies M1401 ion gun

2.3.4 UV-Vis Spectroscopy and Light Detector

Density of an ice film was derived from optical interference measurements with a FilmTek 2000 spectrophotometer. The FilmTek 2000 spectrophotometer has a built-in deuterium and tungsten-halogen light source, covering the ultraviolet and visible light region (wavelength of 190 – 800 nm). The collimated UV-Vis light was transported

through an optical fiber cable and focused onto the gold substrate with sapphire lenses. The specular reflectance spectrum was collected at a 2.5° incidence angle. The reflected light was transported through another optical fiber cable, passed through a 50-μm pinhole and struck a fixed grating which caused wavelength dispersion. A linear charge-coupled-device (CCD) array (2048 pixel) measured the light intensity as a function of the wavelength [4]. In each experiment, a dark spectrum was recorded to measure the stray light from different sources detected by the spectrophotometer. A reflectance spectrum of the gold substrate was recorded before deposition of the film, and a reflectance spectrum of the film was recorded after the deposition. The background spectrum was subtracted from other spectra to remove the effect of the stray light. An example of the reflectance spectra of a water ice film is shown in Figure 2.6. The film thickness, index of refraction and absorbance can be determined by fitting the Fresnel equations for a thin film to the recorded interference pattern using a LabView program created by Teolis [5]. We calculated the density (ρ, in the unit of $g \cdot cm^{-3}$) of the film by a combination of the film thickness obtained from the fitting and the areal mass measured by the QCM. More details are given in Appendix 2 of Teolis's thesis [5] and Westley et al. (1998) [6].

The QCM was turned to face the UV-Vis light source port (45° relative to the doser, Figure 2.1) when measuring the reflectance spectra. However, the QCM was turned toward the Kelvin probe or at some other angles relative to the doser during the deposition. The target underwent rotation between measurements of the reflectance spectra of the gold substrate and the film, and failure to exactly reproduce the initial

position was the main error source for the measured film thickness, and therefore for the calculated density of the film. As the temperature increased, small scale thickness and density variations (e.g., from surface roughness) caused a fraction of the reflected light to be scattered away from the specular direction. In this case, the fitting program can only approximate the effect of scattering on the amplitude of the oscillatioins (baseline adjustment[5]) and the quality of the fit is lower, as shown in Figure 2.6b. The intensity of the oscillation due to interference reduced strongly when there were cracks in the film and the program couldn't fit the experimental data. Films prepared for the optical interference measurements typically had column densities of ~ 1100 ML and the error in the calculated density of each film was $\pm$ 0.02 $g \cdot cm^{-3}$ at temperatures below 100 K and $\pm$0.04 $g \cdot cm^{-3}$ at temperatures from 100 K to 120 K.

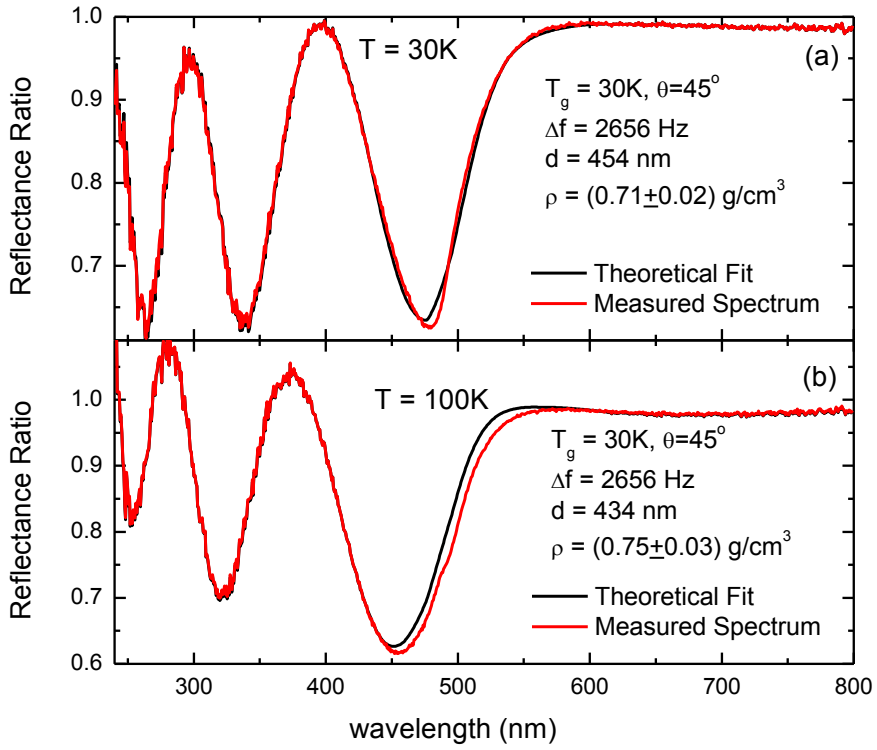

Figure 2.6 (a) The red curve is the UV-Visible reflectance ratio (reflectance of a film to that of the bare substrate) of a water ice film deposited at 30 K at 45° incidence. The black curve is the fit generated using Fresnel's theory, which gives the film thickness of 454 nm. The density of the film was 0.71 g/cm^3, calculated by combining the film thickness with the areal mass measured by the QCM (Δf = 2656 Hz = 1090 ML). (b) The reflectance ratio of the same film at 100 K. The film was heated from 30 K to 100 K at a rate of 4.8 K/minute.

2.3.5 Long-distance Microscope and the Camera

We studied fractures in ice films based on visual characterizations of the film surfaces using a long-distance microscope (Questar QM-100) coupled to a digital camera (Nikon, Coolpix P7000). The microscope has a working distance of 9 inches with a resolution of 3 μm. To be capable of measuring the CPD of the film simultaneously, the QCM was turned to face to the Kelvin probe, while the microscope was set at an angle of 45° relative to the normal of the QCM to examine the surface microstructure of the film, as shown in Figure 2.1. The white illumination for the microscope was set off-specular to enhance the diffusive scattering features. An ice film without cracks is transparent and a cracked film shows scattering patterns (Figure 2.7) [6].

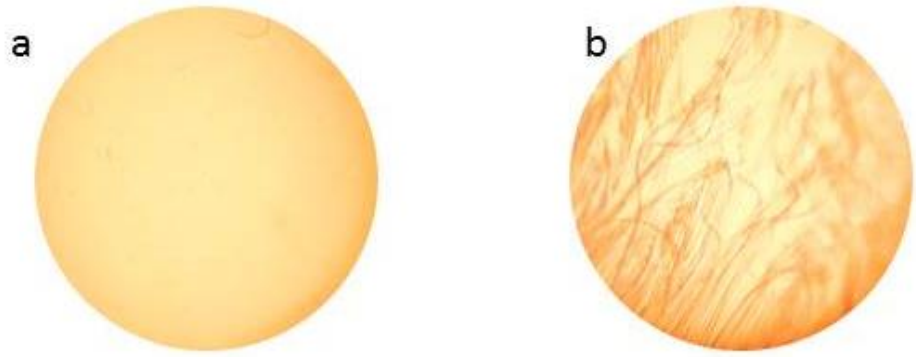

Figure 2.7 Optical microscopy images of a transparent ice film (a) and an ice film with cracks (b).

Reference

[1] M. A. Allodi et al., *Space Sci. Rev*. **180**, 101 (2013)

[2] M. Shi, Ph.D thesis, University of Virginia

[3] K. P, Stevenson, G. A. Kimmel, Z. Dohnalek, R. S. Smith, and B. D. Kay, *Science* **283**, 1505 – 1507 (1999)

[4] U. Raut, Ph.D thesis, University of Virginia, 2009

[5] B. Teolis, Ph.D thesis, University of Virginia, 2007

[6] M. S. Westley, G. A. Baratta and R. A. Baragiola, *J. Chem. Phys*. **108**, 3321 (1998)

Chapter Three

Effects of Microporosity on the Electrical Properties of ASW Films

3. 1 Effect of microstructure on spontaneous polarization in amorphous solid water films

Chapter 3.1 is a manuscript preparing for Physics Review Letters by Caixia Bu, Jianming Shi and Raúl A. Baragiola

Abstract

Amorphous solid water (ASW) films show negative surface potentials if grown at temperatures below 110 K by vapor deposition because of partial alignment of the water molecules during condensation. The negative surface potential increases linearly with film thickness, independently of the type of substrate, decreases with deposition angle and decreases irreversibly by 80 % when annealed at a temperature ~30 K above the deposition temperature. The results show that the polarization is governed by the relaxation of the micropore structure rather than changes in intrinsic dielectric behavior of the water network.

Introduction

Water molecules have a balance of “up” and “down” dipoles in normal high-temperature hexagonal ice, showing no net polarization. However, amorphous solid water (ASW) formed by vapor deposition on substrates below ~130 K, becomes spontaneously polarized via partial alignment of the water molecules, with the surface of the condensate negative with respect to the substrate. The mechanisms involved are unknown; qualitative proposals include resonance energy exchange of the incoming vibrating molecule with the phonons in the condensate [1] and the preferential attraction of protons to the substrate due to an asymmetric distribution of the electric field around the water molecule [2]. The most thorough study of the spontaneous polarization of ASW were done by Iedema et al. [3] using a Kelvin probe to measure the polarization-induced surface potentials in thin films, which they refer to as ferroelectricity. Some of these results were confirmed by us using secondary ion mass spectrometry [4], but a recent study that observed polarization for other condensed polar molecules remarkably failed to detect it in water [5].

Together with small changes in polarization upon crystallization to the cubic phase (> 130 K) [2, 3, 6], the most salient observations pertain the decrease of the polarization voltage with deposition temperature [1, 3] and during annealing [3] of thin ASW films. The thermal relaxation of the dielectric properties, detected previously down to 40 K (and by us to 10 K), were attributed to the “activation” of the dielectric constant from the electronic value $\varepsilon \sim 3$ at low temperatures to $\varepsilon \sim 300$ for rotational alignment close to 100 K [7]. Since it is unlikely that molecules can rotate freely at 40 K, a better alternative is that the film voltages drop with temperature due to the disappearance of the polarization.

We postulated that the thermally induced depolarization is linked to thermally induced changes in the mesoscopic properties of ice, the most salient being the microporosity [8]. Pores of ~1 nm transverse dimension [9] are responsible for huge internal surface areas in ASW, which can reach hundreds [8, 10] of m^2 g^{-1}. Here we report on the spontaneous polarization and thermal relaxation of ASW films formed by vapor deposition at 30 – 110 K, and provide evidence for the essential role of porosity.

Experimental Details

Experiments were performed in an ultra-high vacuum system with a base pressure of 2×10^{-10} Torr. ASW films were deposited from a collimated vapor beam passed through a micro-capillary array [11] or from a diffuse background water vapor onto a gold-coated quartz crystal microbalance [12] (QCM) cooled with flowing liquid helium. The areal mass of the film was measured by the QCM and converted into column density (in units of ML, defined as 1×10^{15} molecules/cm^2) by dividing by the molecular mass. The film thickness d was derived by fitting the Fresnel equations to the interference pattern in the UV-visible optical reflectance [13]. The film density ρ was calculated from the ratio of the mass column density obtained from the QCM to the film thickness and the porosity ($p = 1 - \rho / \rho_c$) was obtained using ρ_c=0.94 g·cm^{-3} for the density of the intrinsic compact ice [14]. The surface potential of the film with respect to the grounded Au substrate was derived from measurements of the contact potential difference with a Kelvin probe [15]. During background deposition, the QCM was rotated to face the Kelvin probe to measure the surface potential of the film continuously during deposition.

Results

Figure 3.1.1a displays evolutions of the surface potentials with film thickness during background deposition at a rate of 0.1 ML/s at different growth temperatures. The surface potential experiences an abrupt change of –0.25 V within the first ~5 ML and subsequently increases linearly with film thickness, at a rate that decreases with growth temperature. Further investigations confirmed the linear relationship between the surface potential and the film thickness also holds if the film is deposited with a collimated vapor beam. The initial change in the surface potential within the first few monolayers occurs when the ASW was deposited onto the Au substrate or to a previously deposited crystalline ice film but not when deposited on a preexisting ASW film, as shown in Figure 3.1.1b. We attribute the initial abrupt change in the surface potential to the change in the work function of the substrate. Above ~5 ML, the evolution of the surface potential shows no dependence on substrate material. Iedema et al. [3] analyzed the degree of polarization of the water molecules in ice films by measuring the contact potential difference after finishing growth of the films and their data sets for the thick (~1×10^5 ML) and thin (~2×10^3 ML) films didn't agree quantitatively, a discrepancy that is in part expected to be caused by the initial abrupt change in the surface potential (Figure 3.1.1) but also by cracks that appear in films with thickness of a few microns [16, 17].

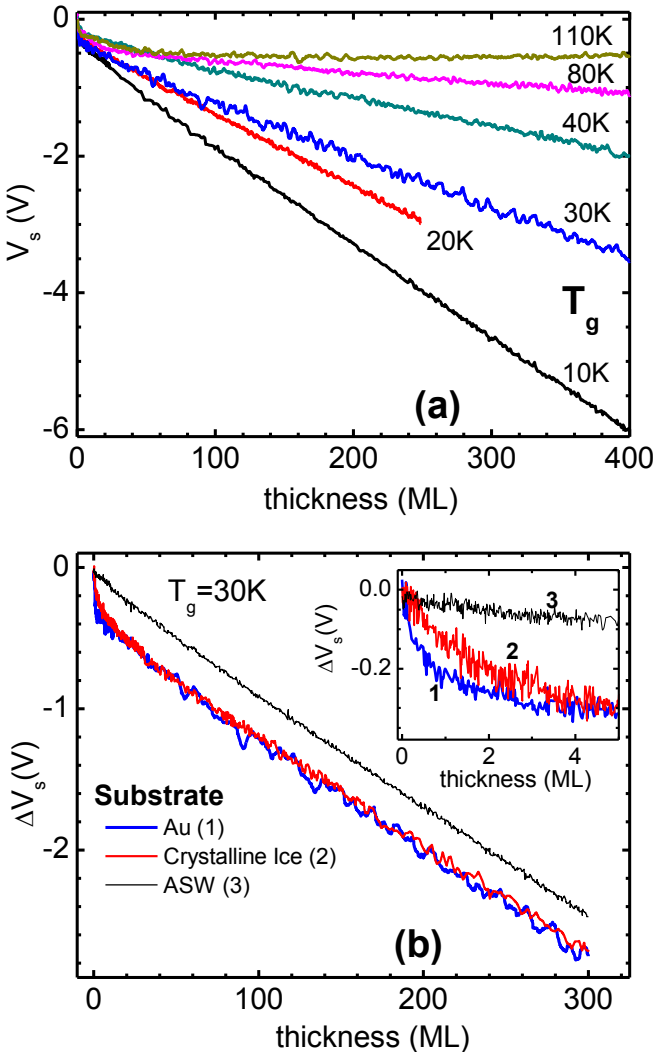

Figure 3.1.1 (a): Dependences of surface potentials on film thickness at different growth temperatures T_g. (b): Change ΔV_s in the substrate potential due to ASW deposition in different substrates at 30 K and at 0.1 ML/s. The substrates are the gold-coated QCM (1-blue): gold plus a 538 ML crystalline ice film (2-red), and gold plus a 514 ML ASW film (deposited at 80 K, 3-black). Inset: evolution of the surface potentials for the first 5 ML.

We tested the hypothesis that the observed surface potential result from capture [18] of spurious external charges during condensation by electrically floating the QCM with respect to the chamber walls to repel stray positive or negative charges. For 510 ML films grown at 30 K, we obtained the same surface potentials within experimental errors for the QCM biased to ±10V or unbiased, confirming that the observed polarization is intrinsic to the ASW films.

To study the dependence of the surface potential on film porosity we grew 1100 ML ASW films at 30 K with the collimated vapor beam at different incidence angles θ, which are known to directly affect the porosity due to shadowing [9, 10, 19]. As shown in Figure 3.1.2, we find that the magnitude of the surface potential decreases with θ, as the porosity increases. Measurements at 80 K lead to the same conclusion.

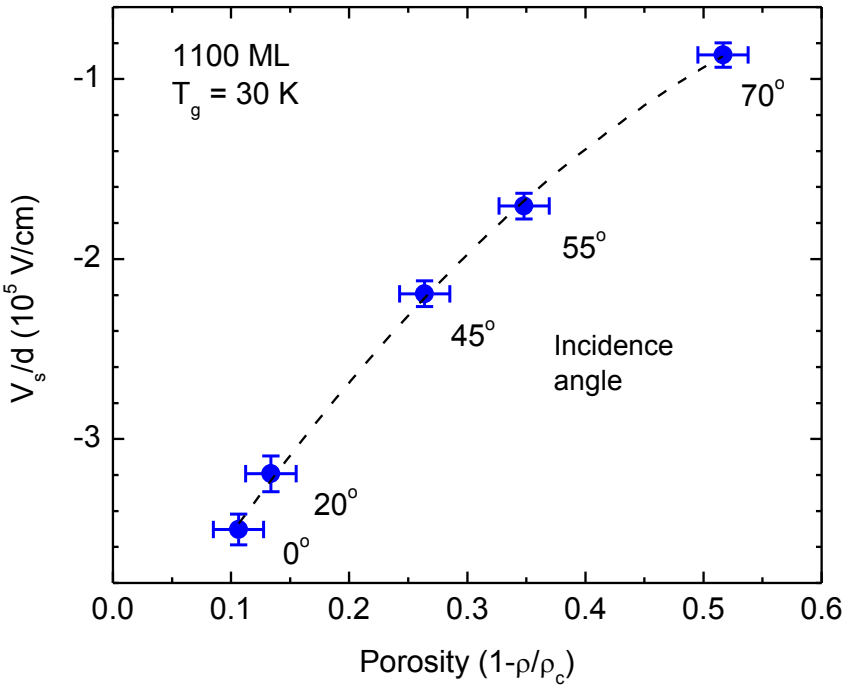

Figure 3.1.2 Dependence of internal polarization field on porosity. Labels are the incidence angle of the vapor flow. The dashed line is to guide the eye.

The inset to Figure 3.1.3 shows that surface potential of ASW films grown at 10 K and above decrease by ~80% when heated to a temperature ~30 K above the deposition temperature, similar to previous work at ≥ 40 K [3]. We found that this evolution of the surface potential with annealing temperature is irreversible and independent of the substrate and film thickness. We notice the common feature that, if a film is heated from the deposition temperature, the surface potential doesn't decrease immediately but after a

lag of ~4 K above the deposition temperature. A likely explanation is the local increase in surface temperature during deposition due to the heat of condensation.

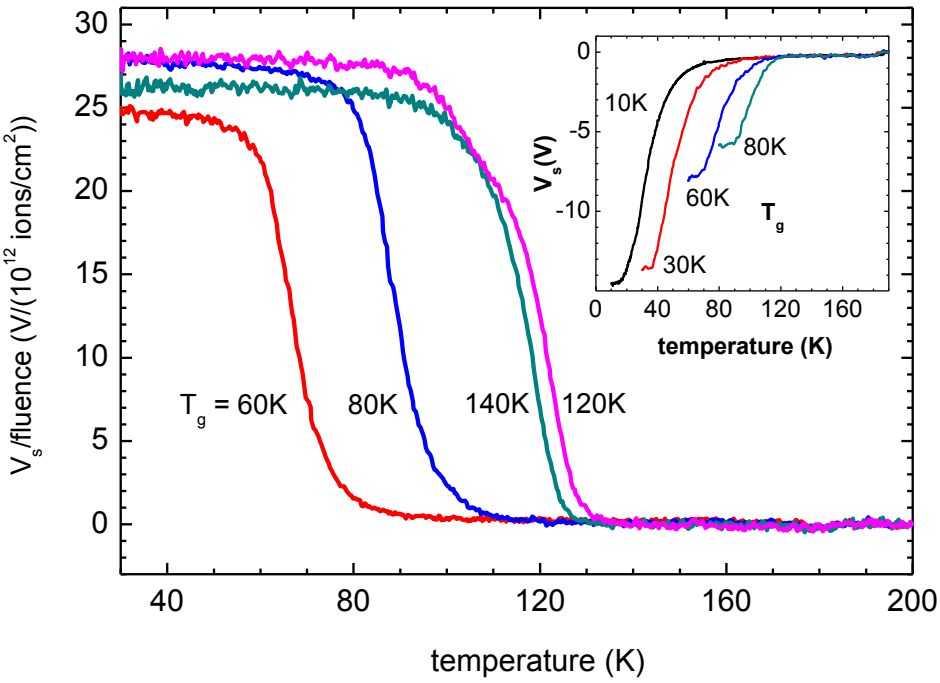

Figure 3.1.3 Surface potential divided by fluence for ASW films grown at 30 K. The films were pre-annealed at the indicated temperature, cooled to 30 K, charged with 500 eV ions to +17 V at 30 K and then heated to 200 K. The inset shows examples of the decay of polarization voltage with annealing for uncharged 1100 ML films grown at temperatures between 10 and 80 K.

As mentioned above, the thermal depolarization has been attributed to a drastic increase in the dielectric constant of the ice [3], even at temperatures below 100 K. To test this hypothesis we measured the dielectric constant by charging, at 30 K, films annealed at different temperatures. We used 500 eV He^+ ions, which deposit a charge per unit area on top of an ice film equal to F the fluence of the irradiation, which we measured with a Faraday cup. The resulting surface potential V_s for a film of thickness d is $V_S = Fd/(\varepsilon\varepsilon_0)$, where ε_o is the vacuum permittivity, and ε is the dielectric constant of the film. Figure 3.1.3 shows that $V_S/F = d/(\varepsilon\varepsilon_0)$ is roughly constant before the film is discharged. We take this as proof that ε is approximately constant below in our temperature range, since changes in d with temperature are small, as shown below.

Figure 3.1.4a shows the effect of film porosity on the thermal relaxation of the polarization. ASW films were deposited at 30 K with the collimated beam at different angles and then heated to 200 K at a rate of 4.8 K/minute. Upon heating, the surface potentials decrease by ~95% at 80 K for the films deposited at small angles (0°, and 45°), and by ~85% for the film deposited at 70°. The normalized curves show that the 70^o film relaxes more slowly than the ones deposited at smaller angles. This correlates with the existence of mesopores (2-5 nm) in the 70° film, in addition to the ~1 nm nanopores [9]. Figure 3.1.4b shows the thickness reduction by thermal compaction of films grown at different incidence angles.

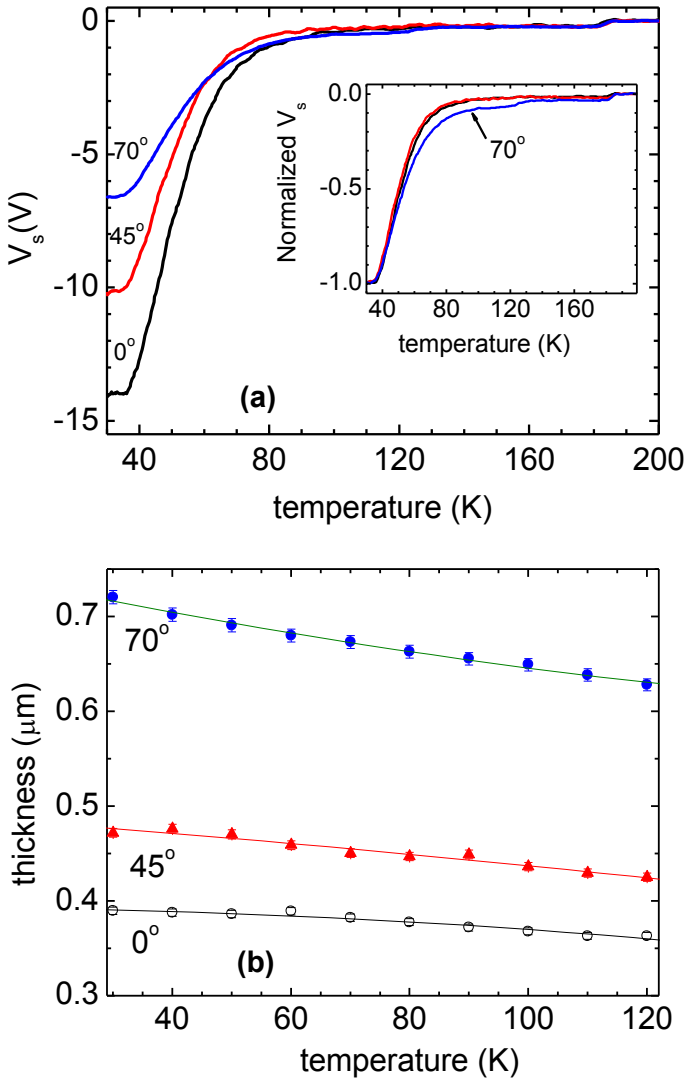

Figure 3.1.4 (a) Decrease of surface potentials while heating (at 4.8 K/min) 1100 ML ASW films deposited at 30 K at different incident angles. Inset: The normalized curves show the distinct behavior of films grown at 70°. (b) Decrease of thickness during heating

When the film is held at a constant annealing temperature, the surface potential decreases with time as shown in Figure 3.1.5. Further investigation indicated that the relaxation rate increases with increasing annealing temperature.

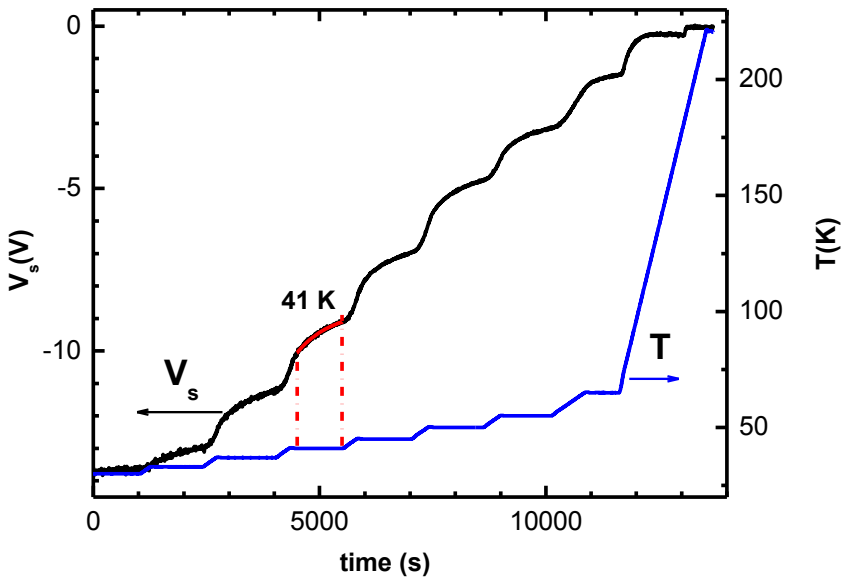

Figure 3.1.5 Decrease of the surface potential of a 1077 ML ASW film deposited at 30 K and stepwise heating to 33 K, 37 K, 41K, 45 K, 50 K and 55 K. The film was held at each annealing temperature for ~1000 seconds and the magnitude of the surface potential decreased with time.

Discussion

The strong dependence of surface potential on the porosity of the films leads us to propose that the spontaneous polarization of vapor deposited ice is related to the microscopic pore structure. In this picture, the surface potential results from polarization of a small fraction of aligned water molecules on the internal surface of the pores, with the oxygen side towards the external surface. The water molecules that can align are most likely the ones with reduced coordination, double and triple, on the walls of the pores [20, 21] which disappear upon annealing at 60 and 120 K, respectively [22].

We can estimate the degree of polarization of the water molecules on the internal surface of the pores. A water molecule in water ice has a permanent dipole 3.1 D (1 D = 3.34×10^{-30} C·m) with the negative end close to the oxygen atom [23]. Therefore, for a perfectly aligned 1100 ML water ice film, one would expect a surface potential of $V_s = 4\times10^3$ V, using ε=3.2 for the dielectric constant [24]. Since the observed surface potential of a film deposited at 30 K at normal incidence is –14 V, only 0.35% of the total water molecules are aligned. The respective gas adsorption area of the film reported [10] is ~ 130 m^2/g, meaning 3.9% of the water molecules are on the walls of the pores. To create the observed surface potential, 0.35/3.9 or 9% of the water molecules on the pore walls are aligned with the oxygen atoms pointing towards the external surface.

Consistent with the proposed model is the dependence of surface potential on deposition temperature shown in Figure 3.1.1. As the deposition temperature increases, the porosity decreases [8], and the internal surface area reduces, resulting in the lower

surface potential. Above ~110 K, thermal depolarization, bulk diffusion and crystallization change the nature of the problem [3].

If the porosity was the only important variable, one would expect an increased surface potential as the porosity increases with incidence angle in contrast to the observation that the surface potential decreases with deposition angle, as shown in Figure 3.1.2. This can be explained by the fact that the polarization field is given by the component of polarization normal to the surface, which decreases as the cosine of the α, the tilt angle of the pore surfaces. In addition, there is a decrease in polarization with incidence angle expected from the increase in the size of the pores with incidence angle [9]. We note that the ballistic deposition simulations [19, 25] suggest that, as the incidence angle (θ) of the vapor beam increases, the tilt angle α is close but smaller than θ. However, these simulations cannot accurately describe the molecular scale diffusion of the condensing molecule and must rely on normalization to experimental porosities. Thus, we must conclude that the dependence of polarization on incidence angle is a competition between (i) tilting of the local polarization of molecules on the pore surface, (ii) an increase in porosity, and (iii) a change in the pore size distribution.

Our model for the polarization in ASW supports the sharp decrease in the surface potential when the ASW is heated (Figures 3.1.3 and 3.1.4a.). Observations with multiple techniques have confirmed that warming ASW at a temperature higher than the deposition temperature compacts the ASW by closing pores. These include the significant decrease (as large as ~90%) [26] in gas adsorption capacity [8, 10], the disappearance of

the infrared bands due to the dangling OH absorption in pore surfaces [20, 21], and the ten-fold decrease in effective ortho-positronium diffusion length in ASW when heating from 50 K to 120 K [27]. In addition, our data in Figure 3.1.4b show a reduction in the thickness of the films when heated from 30 K to 120 K, indicating elimination of pores. Since collapse of the pores is an irreversible exothermal process [28], the surface potential is irreversible once the film is heated.

The morphology of ASW depends not only on the highest temperature the film is heated to but also the thermal path to that temperature. Hessinger et al. [29], by measuring the internal friction, suggested that ASW films annealed over the crystallization temperature (160 K) were more disordered than the films deposited in the crystalline phase. For a given temperature, the film deposited at that temperature has the highest polarization (e.g., the surface potential of the film deposited at 60 K is ~ -8 V, while of the film deposited at 30 K and annealed to 60 K was ~ -2 V), supporting the dependence of the film morphology on thermal path.

It has been reported that the structure of water ice changes with time when held at a constant temperature. Schmitt et al. [17] found that the surface area for gas adsorption decreased with time for the film grown at 77 K and kept at that temperature. Wu et al. [30] suggested reorganization of water molecules at temperatures as low as 50 K. We observed that the surface potential of the film decreases with time if the film is held at a constant annealing temperature (Figure 3.1.5), which is consistent with the reported change in the structure of the film.

Conclusions

In conclusion, we propose that the observed surface potential results from a fraction of aligned water dipoles (~9% if deposited at 30 K at normal incidence) on the internal surface of the pores with the oxygen lone pair electrons preferentially pointing towards the external surface. Depolarization occurs during the collapse of the pores, resulting in the decrease of the surface potential. The effects observed here could have applications to other microporous solids, such as amorphous silica, at higher temperatures.

Acknowledgments

We acknowledge support from the NASA Outer Solar System Program and helpful discussions with U. Raut and E. Mitchell.

References

[1] K. Kutzner, *Thin Solid Films* **14**, 49 (1972)

[2] L. Onsager, D. L. Staebler, S. J. Mascarenhas, *J. Chem. Phys*. **68**, 3823 (1978)

[3] M. J. Iedema, M. J. Dresser, D. L. Doering, J. B. Rowland, W. P. Hess, A. A. Teskouras, and J. P. Cowin, J. Phys. Chem. B 102, 9203 (1998)

[4] J. Shi, M. Fama, B.D. Teolis, R. A. Baragiola, *Phys. Rev. B* **85**, 035424 (2012)

[5] R. Balog, P. Cicman, N.C. Jones, and D. Field, Phys. Reve. Lett. 102, 073003 (2009)

[6] X. Su, L. Lianos, R. Y. Shen, and G. A. Somorjai, *Phys. Rev. Lett*. **80**, 1533 (1998)

[7] O. Dengel, U. Eckener, H. Plitz, and N. Riehl, Phys. Lett. 9, 291 (1964)

[8] E. Mayer and R. Pletzer, *Nature* (London) **319**, 298 (1986)

[9] U. Raut, B. D. Teolis, M. J. Loefffler, R. A. Vidal, M. Fama, and R. A. Baragiola, *J. Chem. Phys.* **126**, 244511 (2007)

[10] K. P. Stevenson, G. A. Kimmel, Z. Dohnalek, R. S. Smith, and B. D. Kay, *Science* **283**,1505 (1999)

[11] N. J. Sack, R. A. Baragiola, *Phys. Rev. B* **48**, 9973 (1993)

[12] M. A. Allodi et al., *Space Sci. Rev*. **180**, 101 (2013)

[13] M. S. Westley, G. A. Baratta and R. A. Baragiola, *J. Chem. Phys*. **108**, 8 (1998)

[14] A. H. Narten, C. G. Venkatesh, and S. A. Rice, *J. Chem. Phys.* **64**, 1106 (1976)

[15] J. Shi, M. Fama, B.D. Teolis, R. A. Baragiola, *Phys. Rev. B* **85**, 035424 (2012)

[16] B. E. Wood, and J. A. Roux, *J. Opt. Soc. Am.* **72**, 720 – 728 (1982)

[17] B. Schmitt, J. Ocampo, J. Klinger, *J. Phys.* (Paris) **48**, CI, 519 – 525 (1987)

[18] R. Balog, P. Cicman, D. Field, L. Feketeova, K. Hoydalsvik, N. C. Jones, T. A. Field and J. P. Ziesel, *J. Phys. Chem. A* **115**,6820-6824 (2011)

[19] Z. Dohnalek, G. A. Kimmel, P. Ayotte, R. S. Smith, and B. D. Kay, *J. Chem. Phys.* **118**, 364 – 372 (2003)

[20] V. Buch and J. P. Devlin, J. Chem. Phys. **94**, 4091 (1991)

[21] B. Rowland and J. P. Devlin, *J. Chem. Phys.* **94**, 812 (1991)

[22] C. Bu, chapter 3.2

[23] E.R. Batista, S. S. Xantheas, H. Jónsson, *J. Chem. Phys.* **109**, 4546 (1998)

[24] P. V. Hobbs, *Ice Physics*, Clarendon Press, Oxford (1974).

[25] A. G. Dirks and H. J. Leamy, *Thin solid films* **47**, 219-233 (1977)

[26] A. Bar-Nun, and T. Owen, *Solar System Ices*, eds. B. Schmitt, C. De. Bergh, M. Festou (Dordrecht: Kluwer) **353** (1998)

[27] Y. C. Wu, A. Kallis, J. Jiang, and P. G. Coleman, *Phys. Rev. Lett.* **105**, 066103 (2010)

[28] J. A. Ghormley, J. Chem. Phys. 48, 503 (1968)

[29] J. Hessinger, and R. O. Pohl, *Journal of Non-Crystalline Solid* **208**, 151 – 161 (1996)

[30] Y. C. Wu, J. Jiang, S. J. Wang, A. Kallis, and P. G. Coleman, Phys. Rev. B **84**, 064123 (2011)

3.2 Ion-induced electrostatic charging and discharging of porous amorphous solid water (ASW) films

Chapter 3.2 is a manuscript prepared by Caixia Bu and Raúl A. Baragiola, pertaining to depolarization seen in chapter 3.1.

Abstract

Studies in this chapter examined the role of porosity, a crucial characteristic of amorphous solid water (ASW), on the electrostatic charging of ASW with an ion beam and the discharging of the deposited charge. Measurements of surface potentials with a Kelvin probe indicate that ASW films have a dielectric constant of ~ 3 at temperatures below 100 K. When an irradiated ASW film is heated, the surface potential of the film sharply decreases at a temperature that depends on the highest temperature the film was once heated to. We ascribe this sharp decrease in surface potential to the actual migration of ions through the film to the substrate and suggest that the migration is facilitated by the collapse of pores, rather than dielectric shield due to a large dielectric constant.

Introduction

Amorphous solid water (ASW) is grown from condensation of water vapor onto cold surfaces (below ~ 130 K), and research on ASW is stimulated by the need of the understanding of the properties of water and properties of this type of ice in astronomical environments [1]. A fundamental topic, studied for decades, and still remained

controversial, is the motion of ions in water ice at low temperatures (< 130 K). Whereas fast proton mobility in crystalline ice is theoretically expected from the Grotthuss mechanism, which suggests that proton tunnels across the hydrogen bond network of water molecules [2] followed by reorientation of the water molecules along the path, experiments with polycrystalline ice films suggested that proton motion is thermally activated when warmed to ~ 120 K [3]. Cowin et al. [4, 5] claimed that ions do not move at all in water ice, crystalline [4] or amorphous [5], at temperatures below 190 K; while Kang et al. [6, 7] concluded that hydronium ions are significantly mobile in water ice above ~130 K with the preference to reside at the ice surface rather than in the interior.

A crucial characteristic of ASW is its nanoscale porosity, presenting an internal surface area of hundreds of m^2/g [8]. Experimental results have confirmed that the porosity of ASW decreases with growth temperature and increases with incidence angle of the vapor flux [8, 9, 10]. Thermal annealing [8, 10] and ion irradiation [11] after condensation of the ASW reduce the porosity, by closing some of the pores.

The microporosity affects most of other properties of ASW; however, earlier studies on motions of ions in water ice had not explicitly taken the porosity into account [2 - 7]. To study effects of the microporosity, we prepared ASW films with various porosities, and then charged the surfaces by irradiation with low energy ions: 500 eV He^+ or Xe^+. The surface potentials of the films and their dependences on growth temperatures and post-irradiation annealing temperatures were studied with a Kelvin probe.

Experimental Details

All experiments were conducted in an ultra-high vacuum system with a base pressure of ~ 2×10^{-10} Torr. ASW films were deposited from a collimated vapor beam [12] onto a gold-coated quartz crystal microbalance (QCM) [13] at low temperatures ($\leq$ 140 K). The areal mass of the film was measured by the QCM and was used to deduce the column density (in units of ML, with one monolayer (ML) defined as 10^{15} molecules/cm^2) by dividing the molecular mass. The thickness of the film (d) was obtained by fitting the Fresnel equations to the interferences pattern in the optical reflectance. The film density (ρ) was calculated from the ratio of the column density obtained with the QCM to the film thickness [14]. The porosity ($p = 1 - \rho/\rho_c$) was calculated using $\rho_c = 0.94\ g \cdot cm^{-3}$ for the intrinsic density of compact ice [15]. Surface potentials of the films were derived from measurements of the Contact Potential Difference (CPD) using a non-contact Kelvin probe [16].

To study the microporosity effects on the transport of charge in the ASW films, we irradiated the films with low energy ions (500 eV He^+, unless specified) from a NonSequitur ion gun at normal incidence with the flux kept at $(0.4\pm0.1)\times10^{10}$ ions·cm^{-2}·s^{-1}. At this energy (500 eV), the ions penetrate about ~0.02 μm in the films (based on the TRIM simulations [17]), much smaller than the thickness of the films; thus the charge they deposited can be thought to constitute a thin surface charge layer. When ions deposit a charge Q on top of an ice film (of thickness d) that is condensed on an electrically grounded metal substrate, a surface potential V_s is created, following

$$V_s = \frac{Qd}{A\varepsilon\varepsilon_o} \quad (1)$$

where A is the irradiated area, ε_o is the vacuum permittivity, and ε is the dielectric constant of the film.

Results and Discussion

A. Evolution of the surface potential with fluence at 30 K

ASW films deposited at low temperatures (T < 110 K) show negative surface potentials because of spontaneous polarization, which was explored in our previous study [18]. We first studied how this initial polarization-induced surface potential evolves as charge accumulates on the surface of the film.

An ASW film (1108 ML) was condensed at 30 K at normal incidence, showing a polarization-induced surface potential of $-(14.3 \pm 0.3)$ V. It was then successively irradiated at 30 K for 30 seconds with 500 eV He^+ ions, and the surface potential of the film was measured after each irradiation. The surface potential, as a function of the accumulated fluence, is shown in Figure 3.2.1. At low fluence where the surface of the film is still negative, the surface potential doesn't follow the linear function with fluence as Eq. (1); at higher fluence where the surface becomes positive, the surface potential of the film increase linearly with fluence, following Eq. (1) but with a negative interception.

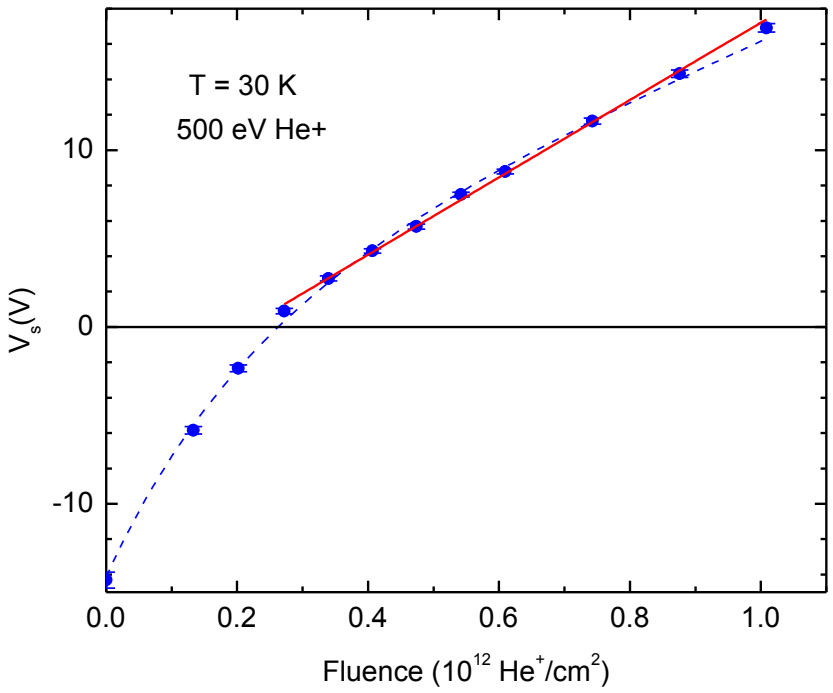

Figure 3.2.1 Evolution of the surface potential of an ASW grown at 30 K with the accumulated ion fluence. The solid-line is a straight-line fit to the positive data points, and the calculated dielectric constant with the fitting slope is 3.3±0.5. The blue dashed-line is to guide the eye.

To explain the observations in Figure 1 we assume that the electric fields duer to spontaneous polarization and electrostatic charging are independent and additive; we'll

return to this assumption below. We use now a picture of the charging process for low energy ions, which is different from that used before for deeply penetrating ions [16, 17]. Low energy ions neutralize at the surface [19], resulting in a positive hole in the solid. Secondary electrons are ejected by different mechanisms [16, 20]; their energy is limited to a few eV due to the large gap (~11 eV) between the top of the valence band of ice and the vacuum level. If the electrons escape into vacuum, additional holes remain in the solid, near the surface (the electron escape depth is a few nm). Additional effects of reflected ions and sputtered ions are negligible in our experiments. Thus, the charge deposited is limited to a very thin surface layer, and the magnitude of the surface charge density is $Q/A = F\,(1+\gamma')$, where γ' is smaller than the electron yield γ if the electrons can return to the surface. At low fluences, the surface is negative because of the spontaneous polarization potential and thus the electrons leave. When the charge build-up produces a positive surface potential of several volts, most of the emitted secondary electrons (whose typical energies are a few eV) return back to the film, $\gamma' = 0$ and the growth rate of the deposited charge is determined by the ion flux, assuming leakage of charge to the substrate is insignificant. Thus, the surface potential of the film increases linearly at higher fluence, following Eq. (1) with $Q/A = F$. From the difference in slope of $V_s(F)$ between the negative and the positive regions of the graph we derive an electron yield $\gamma = 1.8$.

We derive the dielectric constant ε from the slope [$k = \frac{d}{\varepsilon\varepsilon_o} = (1.35 \pm 0.02)\times10^4$ $V\cdot m^2\cdot C^{-1}$] of the positive data points in Figure 3.2.1, where emitted secondary electrons

return back to the film and the deposited charge is determined by the ion fluence. The thickness of the film *d* obtained with interferometry is (0.39±0.02) μm; therefore the calculated dielectric constant is (3.3±0.5), close to established value of ε=3.2 [2] for the high-frequency dielectric constant appropriate in the limit of low temperatures where molecules cannot rotate. The error in the calculated value mainly arises in measurement of the ion fluence. The porosity correction is calculated using the Clausius-Mossotti equation and the measured porosity (8.7%) that agree with earlier work [14].

B. Evolution of the surface potential with annealing temperature

In this section, we report on a series of experiments to find the important variables determining the motion of ions in ASW after irradiation. We present the results followed with discussions.

B.1 Experimental results

a Dependence on fluence

We return to the question of separability of the fields due to the initial polarization and the applied electrostatic charging by studying the dependence of surface potential with annealing temperature. Studies showed that depolarization occurs when an ASW film is warmed, reducing the initial negative surface potential [5, 18]. If the deposited charge atop the film migrates to the substrate while heating, Eq. (1) indicates the ion-induced positive surface potential will also decrease. We conducted experiments to compare these two processes: three ASW films (1120ML) were deposited at 30 K, showing polarization-induced surface potentials of −(13.8±0.2) V. One film was charged to

+(18.6±0.3) V at 30 K, one to −(3.1±0.2) V, and the third one remained non-irradiated. These three films were heated from 30 K to 200 K at a rate of 4.8 K/minute, while monitoring the surface potentials of the films. The evolutions of the surface potentials of these three films upon heating are shown in Figure 3.2.2. The intermediate curve (0.2×10^{10}) is reproduced by 0.77 × the lower curve (polarization) plus 0.37 × the top curve, and the result is indistinguishable from the measured data. The inset of this figure shows that the positive surface potential decreases faster. The surface potential of the film irradiated with intermediate fluence is intermediate between those of the other two films, suggesting that the negative surface potential (induced by polarization during growth) and the positive surface potential (induced by the deposited charge) evolve independently as temperature increases. Further investigation showed that the changes were irreversible; the surface potentials were not reversed by cooling the films.

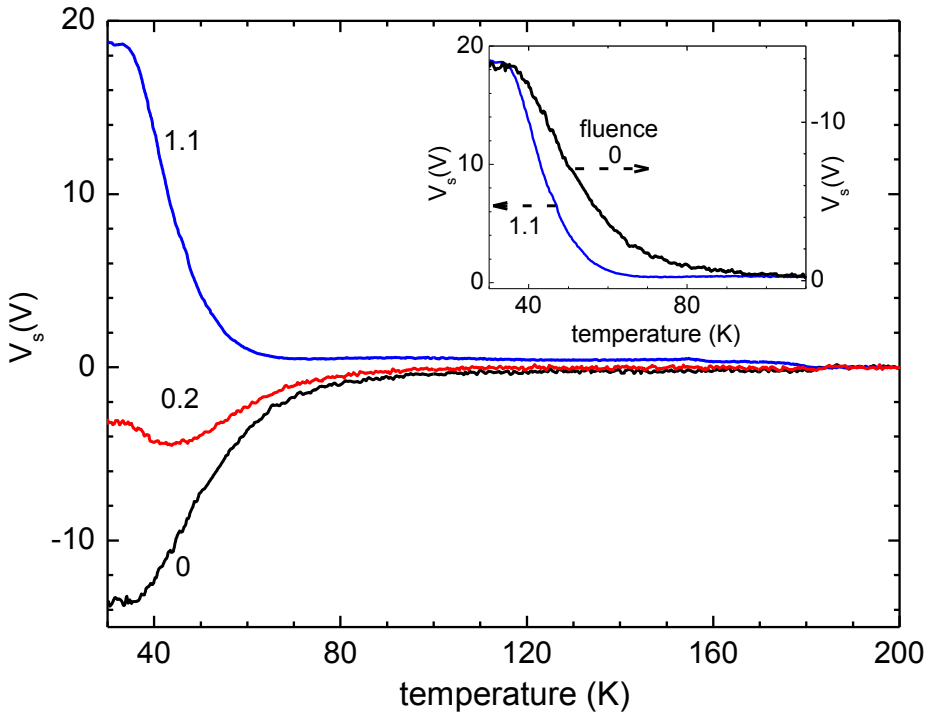

Figure 3.2.2 Evolutions of the surface potentials while heating the ice films from 30 K at 4.8 K/min. The 1120 ML ASW films were condensed at 30 K at 0° (V_s = -14.2±0.3V), and two were charged by 500 eV He^+ at 30 K. The numbers next to each curve are the ion fluence in 10^{12} cm^{-2}. Inset: At the same heating rate, the positive voltage decreases faster than the negative voltage.

b Dependence on deposition angle

It has been confirmed that the porosity of ASW increases with incidence angle of the collimated vapor flux. To achieve different porosities, we deposited ASW films (1100 ML) at 30 K with incidence angles of 0°, 20°, 45°, and 70°. We irradiated these films at 30 K to the same fluence of He^+, and then heated the films to 200 K at a rate of 4.8 K/minute while measuring the surface potentials. Evolutions of the surface potentials with annealing temperature are presented in Figure 3.2.3. Remarkably, the surface potential of the film deposited at 70° decreases by ~84 % at 60 K (from 44.3 V to 7.1 V), less than for films deposited at smaller angles (0°, 20°, and 45°) which decrease by ~ 93% (from 16.8 V to 1.2 V, 19.9 V to 1.2 V, and 24.2 V to 1.9 V, respectively). One possibility causing this observed difference in the surface potential based on Eq. (1) is the difference in film thickness. To correct the effect of the film thickness d, we present the evolution of the electric field (the ratio of the surface potential to the film thickness) in the films with annealing temperature (the inset of Figure 3.2.3). The differences between the curves for different angles are smaller and due to the decrease of the dielectric constant with porosity (angle). Still, the data for 70° show a distinct annealing behavior, likely related to the mesopores [10].

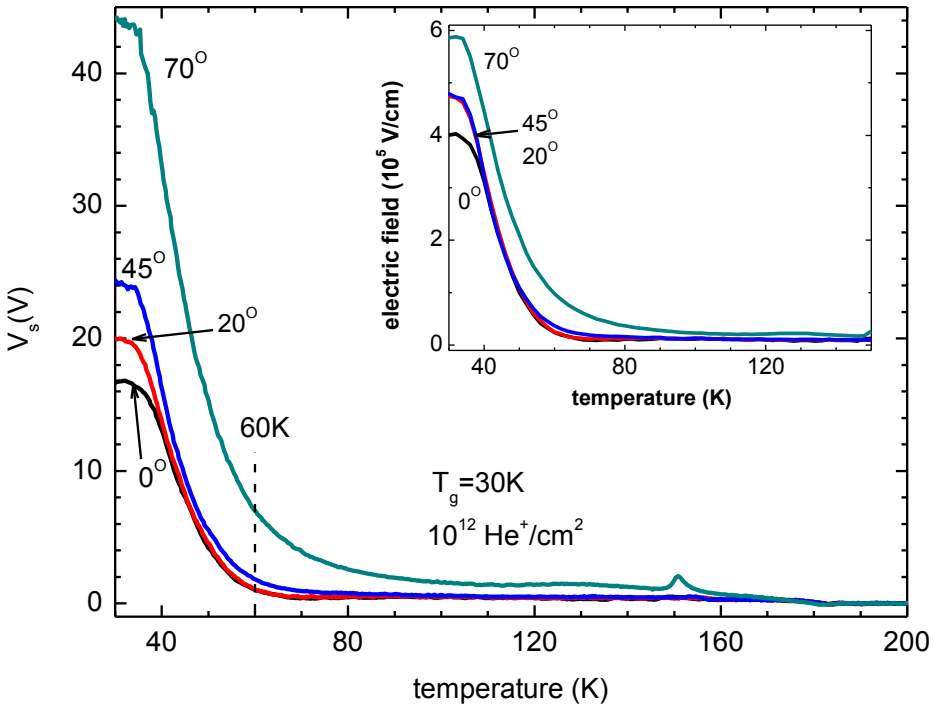

Figure 3.2.3 Evolution of the surface potentials while heating the films from 30 K to 200 K. The films were deposited at 30 K at 0°, 20°, 45°, and 70° (Vs = -13.8 V, -13.2 V, -10.6 V, and -6.3 V, respectively). These films were irradiated at 30 K. At 60 K, the surface potential of the film deposited at 70° decreased by ~84 %, less than for films deposited at smaller angles. Inset: Temperature dependence of the electric field.

c Charging on pre-annealed ASW films

Multiple observations [8, 10] have confirmed that warming ASW reduces the porosity. Therefore, we use the fact that the porosity of ASW decreases with growth and annealing temperatures and measured charging vs. those variables. Four ASW films (1100 ML) were deposited at 30 K at normal incidence, and were warmed to four different temperatures (T_a = 60 K, 80 K, 120 K, and 140 K, respectively) at a rate of 1.8 K/minute, cooled back to 30 K, and then irradiated at 30 K to similar surface potentials (17.0 V, 16.0 V, 16.0 V, and 17.0 V, respectively) with moderate fluences [~0.6×10^{12} ions/cm^2]. These charged films were heated from 30 K at a rate of 4.8 K/minute after irradiation. The ratio of surface potential to fluence in these films was proportional to that of the film thickness to the dielectric constant ($V_s/F \sim L/\varepsilon$). Given that thermal compaction is only ~12% in this temperature range [21], Figure 3.2.4 shows that the dielectric constant is roughly temperature independence. This is in contrast with the assumption of a thermal activation proposed by Cowin et al. [5] where the dielectric constant would increase rapidly with annealing temperature. The calculated dielectric constants for the films in Figure 3.2.4 is (2.5±0.5), taking into account compaction of the films (~12%) [21]. This value is slightly smaller than the value calculated with data in Figure 3.2.1, which can be explained by the effects induced by the slightly negative surface potentials (inset of Figure 3.2.4) of the films after annealing, as discussed above. We interpret the sharp decrease of V_s/F at temperatures somewhat higher than the pre-annealing temperature as leakage of charge to the substrate due to pore collapse.

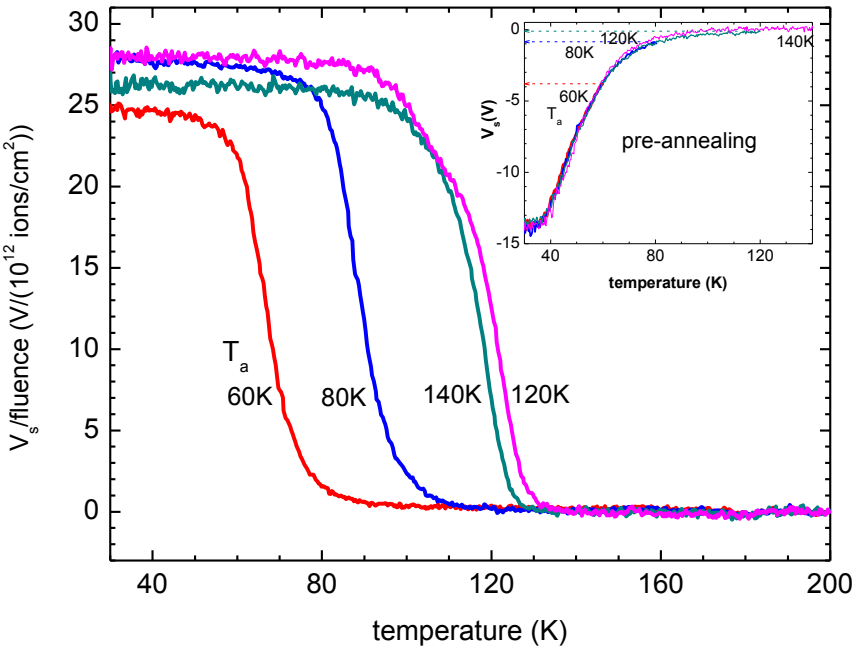

Figure 3.2.4 Dependence of the surface potential (V_s scaled by dividing the fluence in 10^{12}ions·cm^{-2}) with pre-annealing temperature while heating from 30 K to 200 K. The ASW films were deposited at 30 K, pre-heated to 60 K, 80 K, 120 K and 140 K (inset), and then cooled to 30 K. The films were charged to ~17 V at 30 K with fluence between (0.6 – 1.1) $\times 10^{12}$He^{+}/cm^2. For stable charges, V_s/F is proportional to the thickness divided by the dielectric constant and is seen to be relatively independent of temperature before they drop sharply at temperatures somewhat higher than the pre-annealing temperatures. This drop is interpreted as due to the leakage of charge to the substrate.

d Time dependence

We also studied the evolution of surface potential with time at a constant annealing temperature. We deposited two ASW films (1110 ML) at 30 K at normal incidence and pre-annealed one of the two films to 140 K to crystalize the film. Both the ASW and crystalline films, which lacked any polarization voltage, were irradiated at 30 K to comparable surface potentials (16.7 V and 19.5 V, respectively), heated to 37 K at a rate of 1.8 K/minute, and then held at 37 K for 800 seconds. As shown in Figure 3.2.5, the surface potential of the crystalline ice film stays constant while the porous ASW film decreases with time.

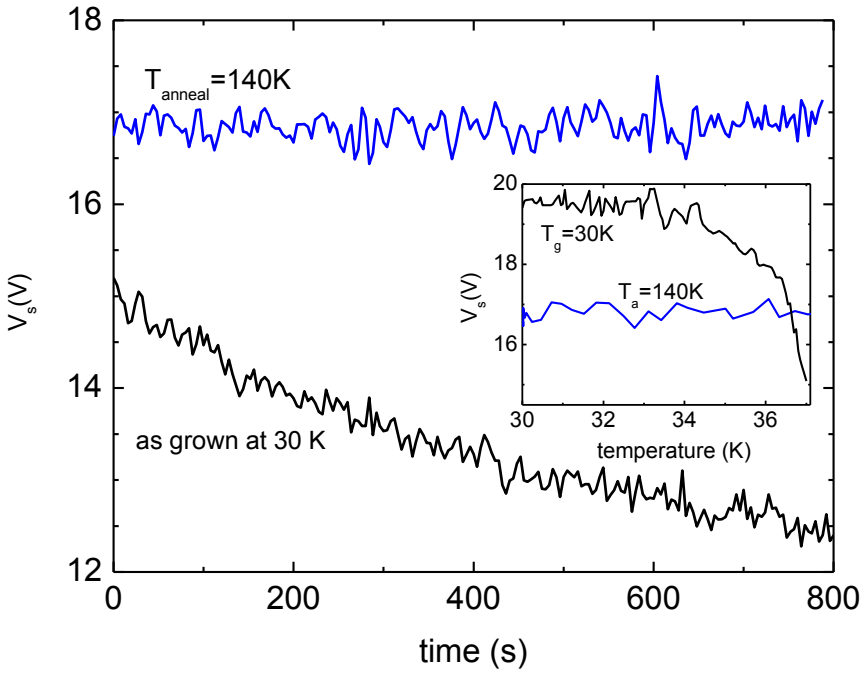

Figure 3.2.5 Evolutions of the surface potentials with time at 37 K. Two ASW Films were deposited at 30 K. One was annealed to 140 K and then cooled back to 30 K. Both films were charged at 30 K and then heated to 37 K. Inset: Initial evolution of the surface potentials during heating the charged from 30 K to 37 K at 1.8 K/min.

e Dependence on irradiation conditions

We irradiated ASW films under different conditions to study possible effects on the transport of deposited charges when heating the films. In one experiment, three ASW films (1120 ML) were deposited at 30 K at normal incidence, having surface potentials of $-(14.2\pm0.3)$ V. They were irradiated at 30 K with 500 eV Xe^+, 500 eV He^+, and 4.4 keV He^+ to similar fluence (1.0, 1.0, and 1.3 respectively, in units of 10^{12}ions/cm^2), and the surface potentials post-irradiation were (22.3 ± 0.3) V, (17.6 ± 0.2) V, and (9.9 ± 0.2) V, respectively. After irradiation, these films were heated to 200 K. It is found that evolutions of the surface potentials with annealing temperature can be normalized to the same pattern (the inset of Figure 3.2.6), independent of irradiation conditions (ion mass and/or energy).

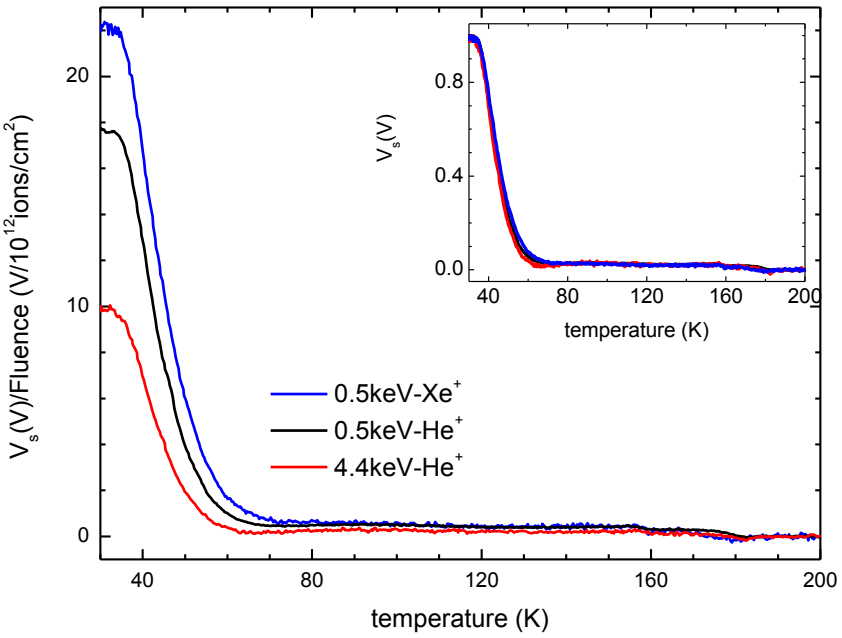

Figure 3.2.6 Evolutions of the surface potentials of 1120 ML films grown at 0° at 30 K when heated from 30 K at 4.8 K/min. The films were irradiated at 30 K with comparable fluence between (1 – 1.3) $\times 10^{12}$ ions/cm^2) but different ions. Inset: the normalized evolution curves.

f Dependence on thermal history

In another experiment, an ASW film (1107 ML) was deposited at 30 K at normal incidence and heated to 140 K, to crystalize the film, which was then cooled to 30 K at a rate of 1.8 K/minute. The cooling was interrupted at 140 K, 120 K and 100 K to irradiate the film to the same fluence; the surface potential of the film after irradiation was (0.0 ± 0.1) V, (1.5 ± 0.1) V, and (17.1 ± 0.3) V, respectively. While cooling, as shown in Figure

3.2.7, the surface potential slowly decreases at temperatures above 100 K, but stayed relatively constant at temperatures below 100 K. When the same film was heated again from 30 K to 220 K, the evolution of the surface potential with annealing temperature was similar to that of a film pre-annealed to 140 K (the inset of Figure 3.2.7), but showed only a mild dependence on other intermediate irradiation temperatures (120 K or 100 K).

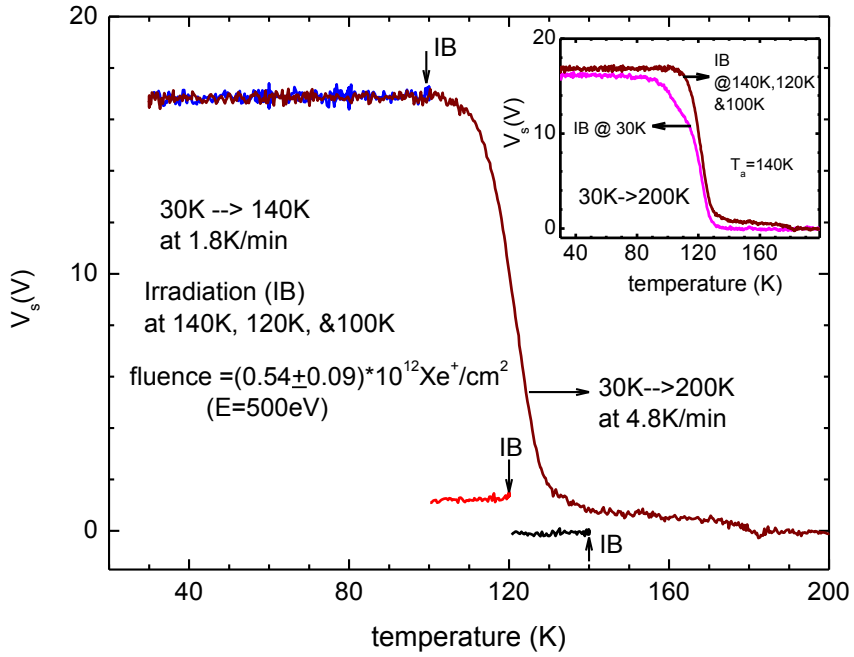

Figure 3.2.7 Effects of irradiation temperature. An ASW film was deposited at 30 K at 0° (-14.0±0.3V), and crystallized at 140 K (-0.05±0.03 V). It was then irradiated sequentially at 140 K, 120 K and 100 K, while cooling back to 30 K (black, red, and blue). Evolution of the surface potential of the charged film upon heating from 30 K to 200 K (wine-red) depends on the highest temperature (140 K) reached by the film (Inset). The purple-line in the inset is the curve for T_a = 140 K from Figure 3.2.4.

a Experiments with sandwiched ions

Recent experimental results suggest that protons have the thermodynamic propensity to reside at the surface of water ice rather than in its interior and slowly migrate from the interior of the water ice to the surface at temperatures below 120 K and this migration is enhanced as temperature increases above 130 K [7]. We prepared double-layered films with charge deposited at different locations of the films, attempting to examine the migration direction of the ions while heating the films. The first double-layered film (Film-I, schematically shown in Figure 3.2.8) was an ASW layer deposited at 30 K on top of a preexisting crystalline ice layer with charge deposited at 30 K atop the ASW layer. At 30 K, surface potential of the crystalline layer was $-(0.02\pm0.01)$ V, $-(6.6\pm0.1)$ V with the ASW overlayer, and $+(14.5\pm0.3)$ V with the deposited charge on top of the ASW overlayer. The second double-layered film (Film-II shown in Figure 3.2.8) consisted of two identical layers as those in Film-I, but with charge deposited at the interfaces of the two layers at 30 K. In this case, the surface potential of the crystalline layer was $-(0.02\pm0.01)$ V, (8.2 ± 0.2) V with charge deposited atop the crystalline layer, and (1.4 ± 0.1) V with the ASW overlayer. Both double-layered films were heated from 30 K to 200 K at a rate of 4.8 K/minute. Upon heating, as shown in Figure 3.2.8, the surface potential of Film-I decreases sharply at ~ 35 K and ~ 100 K, corresponding to the deposition temperature of the top layer and the pre-annealing temperature of the bottom layers respectively, and stays relatively constant between 50 K and 100 K. The surface potential of Film-II sharply increases at ~ 35 K, reaches a plateau and then decreases abruptly at ~95 K. The increase in the surface potential of Film-II at $T < 90$ K is the same

as that of an intrinsic ASW film [18], and we ascribe it to the depolarization in the ASW overlayer of Film-II. At the plateau (95 K), the surface potential of Film-II is 3 V lower than that of Film-I; however, it is expected to be higher or similar to that of Film-I if the deposited charge in Film-II has migrated to the external surface. Therefore, most of the deposited charge must stay in the interior of Film-II below 95 K and leak through the film to the substrate above ~100 K. At the heating rate of 4.8 K/minute, we cannot dismiss the possibility that the deposited charge does slowly migrate to the external surface in Film-II but the rate of migration is much slower than the rate of the leakage.

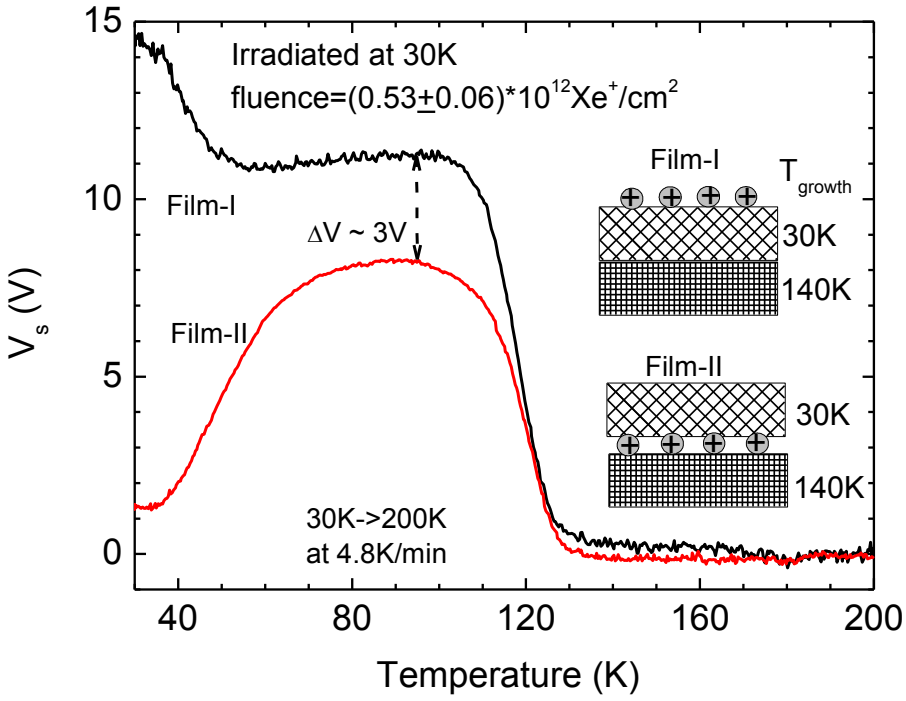

Figure 3.2.8 Evolution of surface potentials while heating the double-layered films. The double-layered films (Film-I & Film-II) consisted of an ASW layer (deposited at 30 K at normal incidence) atop a crystalline layer (pre-annealed at 140 K and cooled back to 30 K). The same fluence of ions were deposited at 30 K atop the ASW layer in Film-I and at the interfaces of the two layers in Film-II. The thickness of each layer was 520 ML.

B.2 Discussion

a Electrostatic charging at 30 K

At low temperatures (< 100 K), water ice's dielectric response to the internal electric field would be limited by high activation barriers to reorientation of water dipoles (0.56 – 0.59 eV in crystalline water ice [2]), giving ε=3.2 [2]. The calculated dielectric constant based on Eq. (1) would move unreasonably far from the established value of 3.2 if the deposited charge leaks to the substrate during irradiation or if the water molecules flip to respond to the ion-induced electric field at the irradiation temperature.

If a film is irradiated with a negative surface potential, the emission of the secondary electrons at low fluence, as discussed above for Fig. 3.2.1, makes the deposited charge flux different from the incoming ion flux. To calculate the dielectric constant of ASW with the measured ion flux, we use the data for the pre-heated films shown in Figure 3.2.4, where the surface potentials of the films were close to ~0 V before irradiation. The calculated dielectric constants for the films in Figure 3.2.4 is (2.5±0.5), taking into account compaction of the films (~12%). This calculated value is slightly smaller than the value calculated with data in Figure 3.2.1, which can be explained by the effects induced by the slightly negative surface potentials (inset of Figure 3.2.4) of the films after annealing. These calculated values of dielectric constant of water films indicate the dielectric constant of ASW at 30 K is close to the established value of 3.2 [2] even if once heated to higher temperatures, in contrast with the large number (> 37) proposed by Tsekouras et al. [5].

Surface potentials of the films at 30 K in Figure 3.2.6 are noticeably different, where identical films were irradiated to the same fluence with different ions. The thickness d in Eq. (1) is the distance between the deposited charge and the metal substrate, which depends on the penetration range of the ions. To estimate the effective distance, we calculate the ionization range of the ions in water ice with the TRIM simulation [17]. The TRIM simulations show that the ionization range is 15 nm (7 nm) in ice film for the 500 eV He^+ (Xe^+), and 105 nm for the 4.4 keV He^+. Thicknesses of the films in Figure 3.2.6 were ~ 400 nm, obtained with interferometry. Therefore, the ratio of the effective thickness (d) of the 500 eV ions to the 4.4 keV ions is $\sim (400-15)/(400-105) = 1.3$, assuming that the deposited charged locate at the end of the ionization trajectory [16]. The corresponding experimental surface potential ratio is $17.6/9.9 \approx 1.7$, different from 1.3. We cannot fully understand this inconsistence yet. One possibility is that the charges are preferentially trapped at the surface of the films. Also, the surface potential of the film irradiated with the 500 eV Xe^+ is about 4.7 V higher than that of the film irradiated with the 500 eV He^+, which cannot be accounted for with the ionization range and probably results from differences in the stopping power of the ions or the emission of the secondary electrons as discussed earlier.

In Figure 3.2.7, as the irradiation temperature changes from 140 K to 100 K, the change in the observed surface potential is attributed to the temperature-dependent ion leakage rate during irradiation [16].

b Charge migration in the ice films

Based on the observed evolutions of the surface potentials with annealing temperature in Figure 3.2.2 – Figure 3.2.8, we come to the conclusion that the decrease in the surface potentials with annealing temperature mainly depends on the microstructure of the pores in the film. We propose that the thermal-induced decrease in the surface potential is caused by the migration of ions through the ASW films to the substrate, which is facilitated by the rearrangement of the low-coordinated molecules on the walls of the pores toward high coordination [22].

The literature [2, 3, 6, 7] on the transport of ions in water ice arrived at the consensus that the ion transport occurs via the 'hop-and-turn' mechanism, in which protons tunnel along the hydrogen bonds and water molecules along the previous proton-transfer path reorient to depolarize the hydrogen bonds. Bjerrum defects, D (L) defects which have two (zero) protons between two adjacent oxygen atoms instead of the usual one proton [4], are considered as the main charge carriers in crystalline ice. The concentration and mobility of both the protons and Bjerrum defects mainly determine the conductivity in crystalline ice. The existence of Bjerrum-like defects in ASW is questionable, though the proton transport in amorphous ice was suggested to be consistent with the 'hop-and-turn' point-defect-based mechanism resembling those of the proton-disordered crystalline ice to some degree [23]. Proton hopping over long distance should only occur when the potential is periodic, and proton-disorder will destroy the periodicity [23].

Molecules in the bulk are in a tetrahedral configuration with four hydrogen bonds, and reorientation of these water molecules requires substantial activation energy (~5 eV) [3] to break the hydrogen bonds. Therefore, reorientation of bulk water molecules is expected to be hindered at low temperatures, and ions are expected to be trapped in the solvation well. However, at the surfaces, both the vacuum-ice interface and the walls of the pores, the tetrahedral configuration is broken and the surface molecules have coordination less than four. It is reasonable to expect that the electrical properties on the surfaces are different from those in the bulk. Our measurements show that the surface potentials of the charged films depend strongly on the microporosity of the films, leading us to the suggestion that the ion transport in ASW is related to the micropore structure.

The deposited external charges tend to migrate to the substrate under the electric field produced by the image charges on the gold substrate (Figure 3.2.9). During heating, the double- and triple-coordinated surface molecules rearrange toward higher (triple or four) coordination (also called ‘collapse of the pores’) and the released surface energy provide the necessary energy to depolarize the surface molecules, opening new ion transport paths along the internal surface resembling the ‘hop-and-turn’ mechanism. The depolarized surface molecules are most likely the ones with reduced coordination [22]. The abundance of these low coordinated molecules in the ASW films at low temperatures and the rearrangement of these low-coordinated surface molecules once the films heated promote leakage of the charges along the walls of the pores at temperatures much lower than in the bulk of water films; thus the surface potential drops sharply. The collapse of the pores resumes only when the film is heated to a higher temperature, consistent with

the observation that the temperature where the surface potential decreases sharply only depends on the highest temperature the film once heated to.

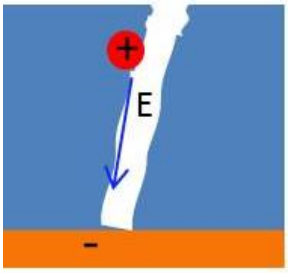

Figure 3.2.9 Schematics draw for the ion transport along the pore walls in ASW films.

It is known that infrared absorption spectra of ASW show enhanced features in the region of the dangling OH bands, DB1 (3720 cm^{-1}) and DB2 (3696 cm^{-1}), assigned to O-H vibration of double-coordinated and triple-coordinated water molecules on the surface of the pores, respectively [22]. To support this model, we take infrared absorption spectra of ASW films during heating.

We present both the surface potential and the integrated areas of both dangling bond features [24] for films (~1100 ML) deposited at 10 K at 45° as a function of annealing temperature in Figure 3.2.10. The results show that the integrated area of the DB1 band

decreases sharply to zero from 10 K to 60 K, resembling the evolution of the surface potential. Measurements for films deposited at other angles (0° and 70°) at 10 K or films deposited at 30 K 45° also confirmed the similarity between the evolution of the surface potential and the area of the DB1 band during heating. Measurements with interferometry show the thickness of the films reduced less than 20 % in the wider range from 10 K to 120 K, a much smaller degree than the surface potential. Based on these results, we suggest that the sharp decrease in the surface potential is governed by the molecular configuration (the dangling bonds, or low-coordinated surface molecules) rather than the porosity (or the film thickness in Eq. (1)).

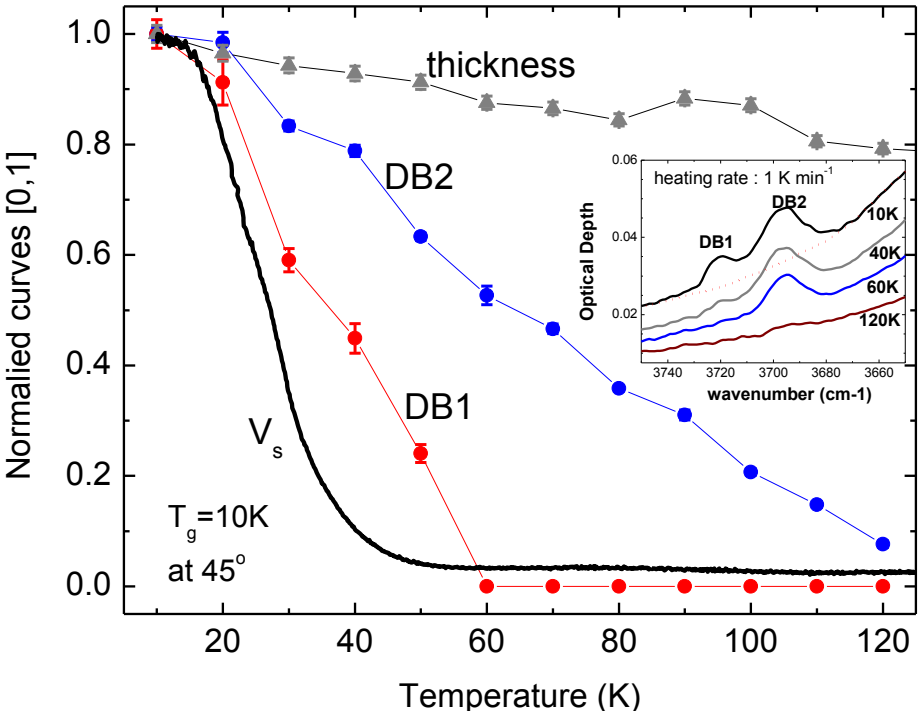

Figure 3.2.10 Comparisons of the film thickness, the surface potential, and the integrated areas of the dangling bonds when heating ASW. An ice film was deposited at 10 K at 45°, and irradiated at 10 K; surface potential and thickness of the film were measured while heating the film at a rate of 1.8 K/minute. The DB1 and DB2 were the integrated areas of the dangling bonds in the infrared spectra (Inset) in Ref.23 where an ice film was deposited at 10 K at 45° and then heated at rate of 1 K/minute. The smooth background (red line) was substrate from each spectrum before calculating the areas. The thickness of these films was ~1100 ML.

We found that depolarization occurs during heating the films due to rearrangement of the surface molecules in Chapter 3. 1 [18]; in this chapter, we show that the thermal-induced rearrangement of the surface molecules also facilitate the transport of ions through the ASW films. With the same heating rate, these two processes relax at different rates as shown in Figure 3.2.2, which cannot be understood at present.

Conclusion

ASW films have a dielectric constant of 3±0.5 at 30–100 K. When an irradiated ASW film is heated, its surface potential decreases irreversibly, and the temperature where the surface potential starts to decrease depends strongly on the highest temperature the film was once heated to. We suggest the decrease in the surface potential is caused by the leakage of the deposited charges through the film to the substrate. Once the films are heated, the pores collapse and the low-coordinated molecules rearranged toward higher coordination, which opens new paths for the motion of the charges along the walls of the pores.

Acknowledgements

This work was supported by NASA Outer Solar System Program. The authors thank Ujjwal Raut and Emma Mitchell for many helpful discussions and for sharing their infrared data.

References

[1] R. A. Baragiola, *Planet Space Sci.* **51**, 953 (2003)

[2] P. V. Hobbs, *Ice Physics* (Clarendon, Oxford, 1974)

[3] P. J. Wooldridge and J. P. Devlin, *J. Chem. Phys.* **88**, 3086 (1988)

[4] J. P. Cowin, A. A. Tsekouras, M. J. Iedema, K. Wu and G. B. Ellison, *Nature* 398, 405 (1999)

[5] A. A. Teskouras, M. J. Iedema, and J. P. Cowin, *Phys. Rev. Lett.* **80**, 26, (1998)

[6] W. Lee, P. R. Lee, Y. K. Kim and H. Kang, *J. Chem. Phys.* **127**, 084701 (2007)

[7] E-S. Moon, C-W. Lee and H. Kang, *Phys. Chem. Chem.Phys.* **10**, 4814 (2008)

[8] E. Mayer and R. Pletzer, *Nature* (London) **319**, 298 (1986)

[9] K. P. Stevenson, Greg A. Kimmel, Z. Dohnalek, R. Scott Smith, and Bruce D. Kay, *Science* **283**, 1505 (1999)

[10] U. Raut, M. Fama, B. D. Teolis, and R. A. Baragiola, *J. Chem. Phys.***127**, 204713 (2007)

[11] U. Raut, B. D. Teolis, M. J. Loeffler, R. A. Vidal, M. Fama, and R. A. Baragiola, *J. Chem. Phys.***127**, 244511 (2007)

[12] N. J. Sack, R. A. Baragiola, *Phys. Rev.B* **48**, 9973 (1993)

[13] M. A. Allodi et al., *Space Sci. Rev.* **180**, 101 (2013)

[14] M. S. Westley, G. A. Baratta and R. A. Baragiola, *J. Chem. Phys.* **108**, 8 (1998)

[15] A. H. Narten, C. G. Venkatesh, and S. A. Rice, *J. Chem. Phys*. **64**, 1106 (1976)

[16] J. Shi, M. Fama, B.D. Teolis, R. A. Baragiola, *Phys. Rev. B* **85**, 035424 (2012)

[17] Ziegler and J. P. Biersack, SRIM 2003, Stopping and range of ions in matter, 2006 (available at www.srim.org)

[18] C. Bu, J. Shi, and R. Baragiola, in process

[19] R.A. Baragiola, in *Low Energy Ion-Surface Interactions*, edited by J. W. Rabalais (Wiley, New York, 1994), Chap. 4.

[20] J. Shi, M. Fama, B. D. Teolis, R.A. Baragiola, *Nuclear Instrument and methods in physics research B* **268**, 2888-2891 (2010)

[21] J. B. Bossa, K. Isokoski, M. S. de Valois, and H. Linnartz, Astronomy and astrophysics

[22] V. Buch and J. P. Devlin, *J. Chem. Phys.* **94**, 4091 (1991)

[23] M. Fisher, and J. P. Devlin, *J. Phys. Chem.* **99**, 11584 – 11590 (1995)

[24] Infrared spectra taken by Emma Mitchell in the same laboratory

Chapter Four

Effects of Cracks on the Electrical Properties of ASW Films

4.1 Spontaneous cracking in amorphous solid water (ASW) films and its effects on the electrical properties

Abstract

Amorphous solid water (ASW) grown by vapor deposition at low temperatures (below about 130 K) crack spontaneously during growth above a critical thickness due to intrinsic tensile stresses. We imaged the cracking and studied its effects on the spontaneous dielectric polarization and transport of charge deposited with an ion beam. We found that the critical thickness for cracking increases as the deposition temperature increases and as the incidence angle of the vapor flux increases. Measurements of surface potentials of the cracked films with a Kelvin probe indicate that depolarization occurs during cracking. If the cracked films are heated, the cracks hinder the depolarization and motion of ions through the films at temperatures below 100 K.

Introduction

Water ice, in the amorphous or cubic phase, is the principal constituent of the surfaces of many satellites and rings in the solar system [1, 2]. Water ice films grown by vapor deposition on cold substrates (< ~130 K) [3], also called amorphous solid water

(ASW) films, serve as laboratory analogues of interstellar ice. A crucial characteristic of the ASW films is their microporosity, which strongly depends on deposition conditions [4, 5] and the sequent processing [6]. The microporosity affects most other properties of the ice films, e.g., gas adsorption ability [4], thermal properties [7], internal friction [8] and the electrical properties discussed earlier chapters of this thesis. However, the microporosity does not contribute appreciably to optical scattering, since pore dimensions (width < 2 nm) [4] are much smaller than optical wavelengths. Therefore, laboratory-prepared thin ASW films are transparent and scatter very little light. Cracks, wide boundaries between particles, can strongly scatter light, making the ice films look frosty. There are scattered reports that ice films may crack during growth [9] or when heated over the phase transformation temperatures, indicated by a transition from transparent to frosty appearance [10]. The mechanism for cracking is poorly understood. Sivakumar et al. [11] reported that films deposited at 110 K broke up when heated or cooled, suggesting that stresses from a mismatch between the thermal expansion of the film and the substrate caused cracking. However, different studies point to an effect caused by a phase transformation at higher temperatures. Ghormley and Hochanadel [12] found cracking during heating up to ~200 K, and suggested the cracking was possibly related to conversion from cubic ice to hexagonal ice. Westley et al. [10] found that cracking starts at 150 K, but the frosty appearance develops fully at ~200 K.

In this study, we detected the onset of cracking in the ASW films, measured the critical thickness at which the cracking onset occurred, and studied the dependence of the critical thickness on both the deposition temperature and the incidence angle of the vapor

beam. Effects of the cracks on the electrical properties of the ice films, without/with cracks and upon heating, were studied by measuring the surface potentials of the films.

Experimental details

Experiments were conducted in the same ultra-high vacuum system shown in Figure 2.1 with a base pressure of ~2×10^{-10} Torr. Films were deposited onto a gold-coated quartz crystal microbalance (QCM) [13] cooled with flowing liquid helium. The column density (n, in units of ML, with one monolayer (ML) defined as 10^{15} molecules/cm^2) of the deposited film was derived from the resulting change Δf in the QCM frequency:

$$n = -\frac{s}{10^{15}\times M}\times \Delta f \quad (1)$$

where M is the molecular mass and $s = 1.227\times10^{-8}\ g\cdot\ s\cdot\ cm^{-2}$ is the Sauerbrey constant [13]. The thickness of the film (d, in the unit of cm) was calculated by

$$d = -\frac{s}{\rho} * \Delta f \quad (2)$$

where ρ is the corresponding film density obtained with interferometry [10, 14].

ASW films were deposited from high-purity water vapor passed through a collimating micro-capillary array doser [15]. The incidence angle of the collimated vapor beam could be varied to produce films with different porosities by rotating the sample [5]. The deposition rate was controlled within (1.7±0.2) Hz/s = (0.7±0.1) ML/s.

During growth, the frequency of the QCM decreased linearly with the column density of the film, as indicated in Eq. (2), and jumped abruptly when the column density increased to some point. Microscopic images of the film, taken with a Questar long-distance microscope (coupled to a digital camera, at a distance of 9 inches, and with a resolution of ~ 3μm), indicated that the film fractured at this point. Eq. (2) was no longer held when the column density exceeded this point. We used this abrupt change in the QCM frequency as an indicator of the onset of cracking; though we couldn't provide detailed reasons causing this change (One possibility was the released stress as discussed later.). Growth of the films was stopped when the abrupt change in the QCM frequency was observed. The critical thickness was still calculated with Eq. (2), but with the value of Δf immediately before the onset of cracking. Microscopic images of the surfaces of the cracked films were taken by the Questar long-distance microscope. Surface potentials of the films were derived from measurements of the contact potential difference (CPD) with a Kelvin probe [16].

To study the effect of cracking on the motion of ions in the water ice films, we irradiated the films with low energy ions (500 eV, He^+) from a NonSequitur ion gun at normal incidence for ~270 seconds, to a fluence of ~1×10^{12} ions·cm^{-2}. At this energy, the ions penetrate ~0.02 μm (calculated with TRIM simulations [17]), much smaller than the thickness of the films; thus the charge they deposit can be thought to constitute a thin surface charge layer.

Results

A. Critical thickness and its dependence on deposition conditions

We first studied the dependence of the critical thickness on deposition temperature by depositing ASW films at T_g = 10 K, 30 K, and 50 K with the molecular beam at normal incidence. We terminated the deposition of the film when the QCM indicated the onset of cracking by an abrupt change in the frequency. Microscopic images of the cracked films are shown in Figure 4.1.1 (top panel). As the deposition temperature increases, cracks develop from small-scale, dense, and ramified patterns to large, sparse, and nearly-straight lines.

A second group of ASW films was grown at 30 K with incidence angles of 0°, 45° and 55° until cracking occurred, to study the dependence of the critical thickness on film porosity [5]. For incidence angles larger than 55°, the critical thickness was too large (>10 μm for 70°) to be measured using this experimental setup. As the incidence angle increases, the developing tendency of the cracks is less obvious, showing slightly smaller-scale and less line-like cracks at larger incidence angle (Figure 4.1.1, bottom panel).

Measurements of the surface potentials are presented in Figures 4.1.2a & 4.1.2b, as a function of film thickness. It is found that the amplitude of surface potentials increases linearly with thickness and abruptly decreases when the films crack. The cracking-induced change in the amplitude of the surface potentials decreases with increasing deposition temperature (Figure 4.1.2a) and incidence angle (Figure 4.1.2b). The critical

thickness, where a film cracked, increases with increasing deposition temperature (Figure 4.1.2a) and incidence angle (Figure 4.1.2b).

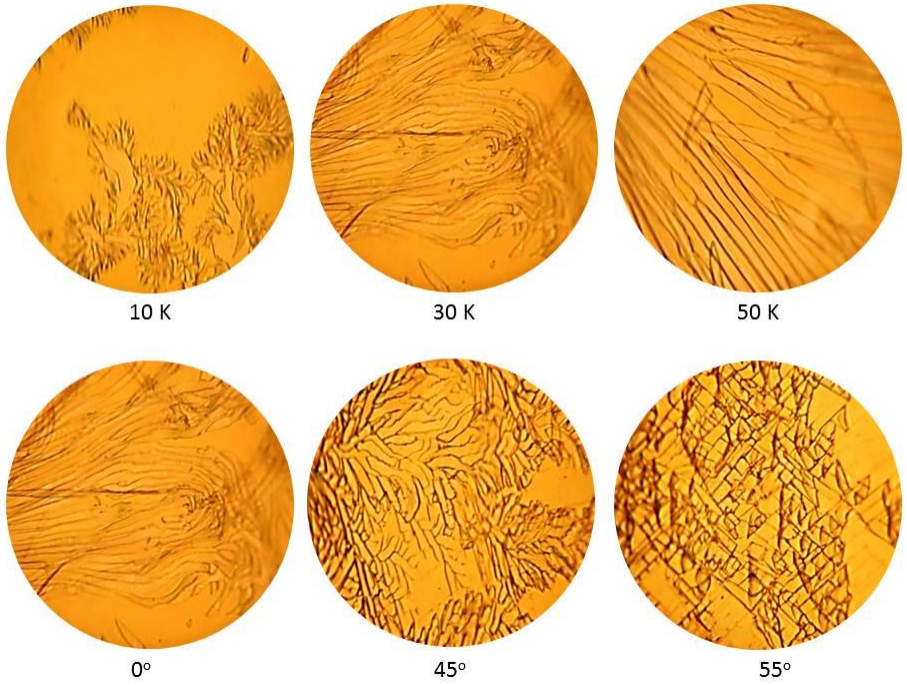

Figure 4.1.1 Microscopic images of cracks in ice films immediately after the onset of cracking. When the films cracked, depositions were stopped, and images were taken. The field of view is 1.4 mm-dia. The geometry of the cracks depends on the deposition conditions. Top: ASW films were deposited at normal incidence at 10 K, 30 K, and 50 K. Bottom: ASW films were deposited at 30 K at incidence angles of 0°, 45°, and 55°.

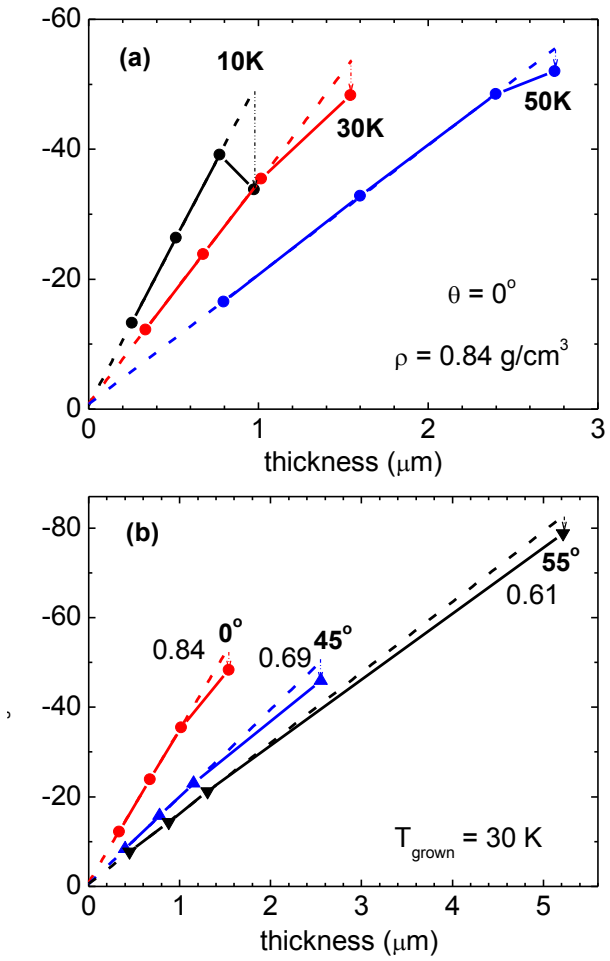

Figure 4.1.2 Cracking of ASW films decreases the negative surface potential (solid lines). Surface potentials increase linearly with thickness without cracks (dashed lines) and abruptly decrease when the films crack (the last data point on each solid line). (a): ASW films deposited at incidence angles of 0° at 10 K (solid black), 30 K (solid red), and 50 K (solid blue). (b): ASW films deposited at 30 K at incidence angles of 0° (solid red), 45° (solid blue) and 55° (solid black). The numbers next to the incidence angle are the film densities were obtained with optical interferometry.

B. Evolution of the cracks upon heating

We deposited an ASW film at 30 K at 55°, discontinuing the deposition at the onset of cracking (the critical thickness was 4.9±0.1 μm). The cracked film was heated from 30 K to 220 K at a rate of 4.8 K/minute, while simultaneously examining the surface of the film with the optical microscope. We recorded cracks as they continuously developed with temperature, and present images of the identical location at 30 K and 90 K in Figure 4.1.3. Image field of view was (1.4±0.1) mm-dia. A few initial cracks were observed at 30 K, and most of the areas between the cracks remained transparent; by the time the sample reached 90 K, the initial cracks became more prominent and new cracks appeared.

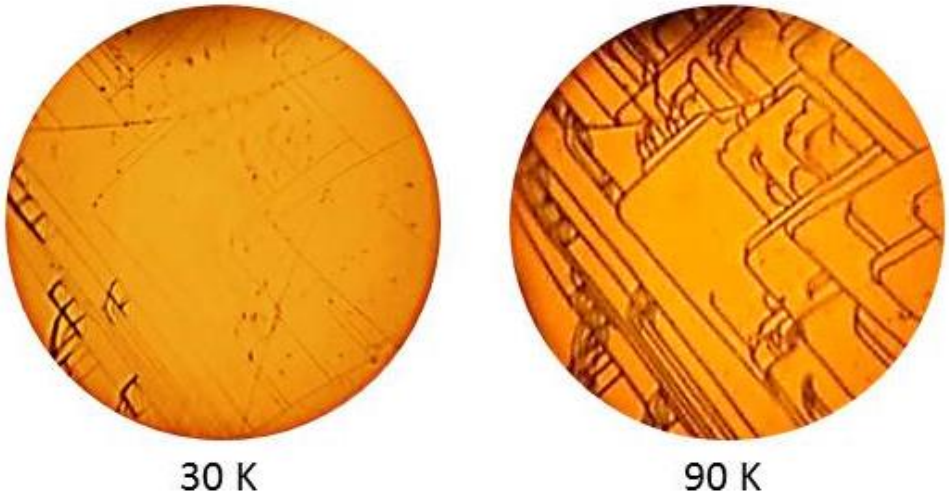

Figure 4.1.3 Microscopic images of a cracked film at 30 K (left) and 90 K (right). The film was deposited at 30 K at 55° till onset of cracking. Then the growth was stopped and the film was heated at a rate of 4.8 K/min, while imaging the same spot of the film surface. The field of view is 1.4 mm-dia.

C. Evolution of the surface potentials upon heating

Two cracked films were prepared at each deposition temperature (10 K, 30 K and 50 K) at normal incidence. One film was directly heated from the deposition temperature to 220 K at a rate of 4.8 K/minute, to study the crack-induced effect on depolarization with annealing temperature. The other film was first irradiated at the deposited temperature for 270 seconds to a fluence of $(0.8\pm0.1)\times10^{12}$ $He^{+}\cdot cm^{-2}$, and then heated at 4.8 K/minute to 220 K, to study the effect of the cracks on the motion of ions while changing the annealing temperature. The results are presented in Figure 4.1.4a and Figure 4.1.4b. We conducted similar experiments with cracked films prepared at 30 K at different incidence angles (0°, 45° and 55°) with the results presented in Figure 4.1.4c and Figure 4.1.4d.

Compared to the thin films (1100 ML, transparent), the amplitude of the surface potentials in the cracked films stays at a higher level and has multiple sharp decreasing temperature ranges while heating from the deposition temperature to 220 K. The first decreasing range was within temperatures about 30 K above the deposition temperature, similar as the case in the thin films. However, the amplitude of the surface potentials in the cracked films had other two decreasing ranges: one was between 90 K and 130 K, and the other was between 180 K and 190 K within which the surface potentials decreased to zero. Outside these three ranges and below 190 K, the amplitude of the surface potentials in the cracked films decayed at much slower rates than those in these three ranges.

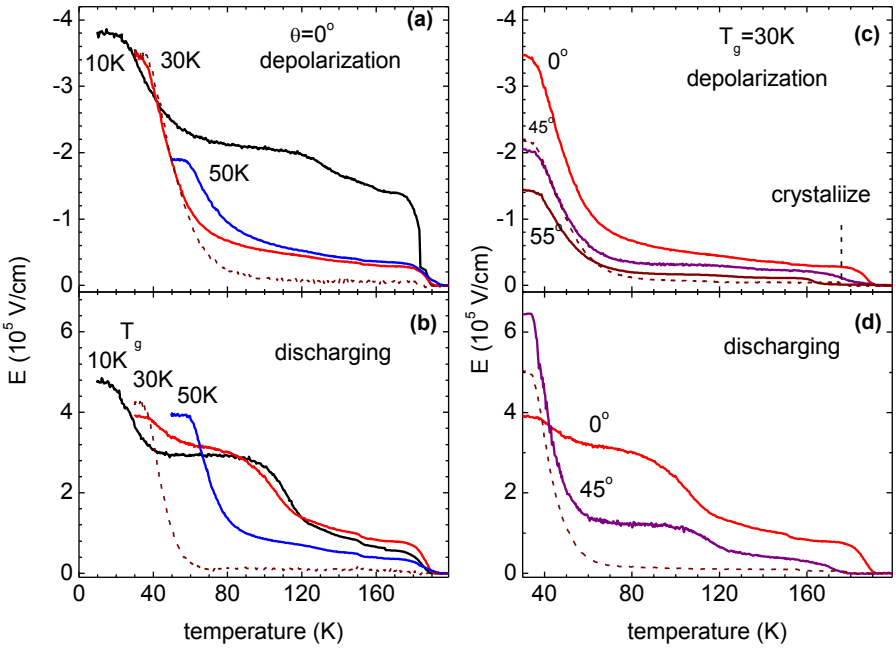

Figure 4.1.4 Evolution of electric fields (E= V_s /*d*, where V_s is the surface potential and *d* is the film thickness) of cracked films (solid lines) upon heating. Cracked films were prepared at 0° at 10 K, 30 K, and 50 K **(a, b)** or at 30 K at different angles of incidence: 0°, 45° and 55° **(c, d)**. The thicknesses of the cracked films were the corresponding critical thicknesses shown in Figure 4.1.3. Films were heated from the deposition temperatures to 220 K at 4.8 K/min. The dotted lines are the results for thin films (1100 ML, < 0.5 μm), prepared as the corresponding cracked films except with smaller thicknesses. The fluence for (**b, d**) was 1.0×10^{12} He^{+}/cm^{2}. No surface potential data were available for a charged cracked film deposited at 30 K at 55°, since the expected voltage was outside the range of our Kelvin probe.

Discussion

A. Mechanism for cracking

We note that tensile stresses usually develop during deposition of thin films when their density is lower than the compact solid and the films are anchored into a rigid substrate [18]. In the absence of significant diffusion (as in the case of ASW below 100 K), the film can relax normal to the surface but not radially. Microscopically, the stress results from the short-range attractive interaction between the walls of voids or pores (~1 nm wide nanopores in the case of ASW [6]). Thermal vibrations assist in snapping the walls of the pores together closing the pores. As shown in Figure 4.1.5, this is similar to the zipping mechanism invoked for stress formation and island coalescence during vapor deposition of thin films via the Volmer-Weber mechanism [19, 20, 21], but occurs through the film thickness, not just between nearby surface islands. In this picture, cracks are formed due to fissures near the ice-substrate interface when, according to the Griffith criterion [22], enough energy is available to generate new crack surface. Thus, a minimum thickness of stressed film is required for the initial flaw to propagate into a crack:

$$L = \frac{2\gamma E}{\pi\sigma^2} \tag{3}$$

where γ is the surface energy, E is Young's modulus, and σ the film stress.

Although this equation cannot be evaluated for ASW since the individual parameters are unknown, it can be used to explain why the critical thickness increases at high

temperatures when the deposited films are more compact (smaller σ). The increase of L with deposition angle is due to a reduced radial stress because of the tilt of the pores [23].

The optical scattering due to the cracks is possibly connected with the brightening of ice films under ion irradiation, which was observed in previous studies [24, 25], that can be due to cracks produced by stresses generated during irradiation [6].

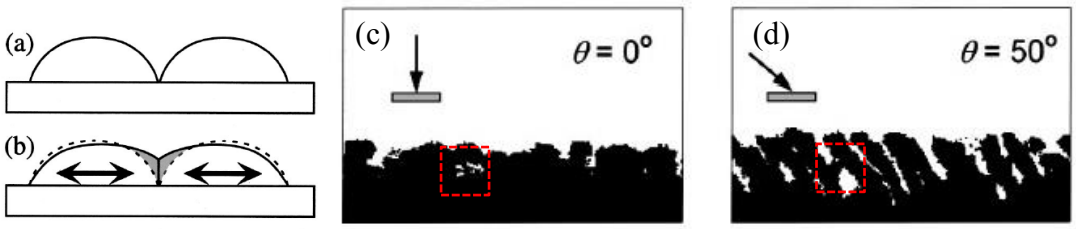

Figure 4.1.5 (a, b) Zipping mechanism for stress formation [Ref.19]. Surface islands zip together (from (a) to (b)), forming a gain boundary and creating tensile stresses. The shaded region is formed entirely via elastic deformation, not mass transport. (c, d) Ballistic deposition simulations of water ice [Ref. 23]. Stresses generate when the walls of the pores snap together (for example, the regions inside the red box), following similar mechanism shown in (a, b) and occurring through the film thickness. The angles are the incidence angle of the vapor beams.

B. Cracking-induced effects on electrical properties

An ASW film shows a negative surface potential during growth because a fraction of the water molecules are aligned [26]. This negative surface potential increases linearly with thickness if the film doesn't crack, and decreases when the film is heated [14, 26]. Surface potential measurements in Figures 4.1.2 show that the amplitude of the surface potentials decreases when the films crack, indicating that depolarization occurs during cracking. As discussed earlier, the films are under stress. The strain energy is released around the cracked sites as the film cracks, and the released energy relaxes the nearby molecules, disturbing the alignment of the dipoles thereby reducing the surface potential. The observation that the crack-induced decrease in the amplitude of the surface potentials (the difference between the solid line and the dashed line at cracking points in Figure 4.1.2) reduces with increasing deposition temperature (Figure 4.1.2a) or incidence angle (Figure 4.1.2b) is in agreement with the fact that tensile stresses decrease with increasing deposition temperature (due to increasing molecular relaxation during condensation) or incidence angle (possibly due to increasing distance between the walls of the pores).

Upon heating, in contrast to the thin films, a much larger fraction of the surface potential is retained at temperatures as high as 150 K in the cracked films, as shown in Figure 4.1.4 (a, b, c, d). As discussed in Chapter Three, the thermal relaxation of the surface potentials (resulting from the polarization or electrostatic charging) relies on the low-coordinate surface molecules along the walls of the pores and their rearrangement toward higher coordination during heating. When the films crack, some of the (depolarization/discharging) paths are broken by the cracking-induced voids (as

schematically shown in Figure 4.1.6). The aligned dipoles or the deposited charges are trapped at the voids, a possible explanation for the larger fraction of the surface potentials in the cracked films. At temperatures above 100 K, molecular diffusion is activated, which resumes some paths for the depolarization of the aligned dipoles or for the migration of the charge to the substrate, reducing the surface potentials sharply. A fraction of the trapped dipoles and charge is in deeper traps (schematically shown in Figure 4.4.6) and decays at temperature between 120 K and 160 K. At ~160 K, massive movements of the molecules during phase transformation facilitate the relaxation of the dipoles or charge, resulting in the disappearance of the surface potentials.

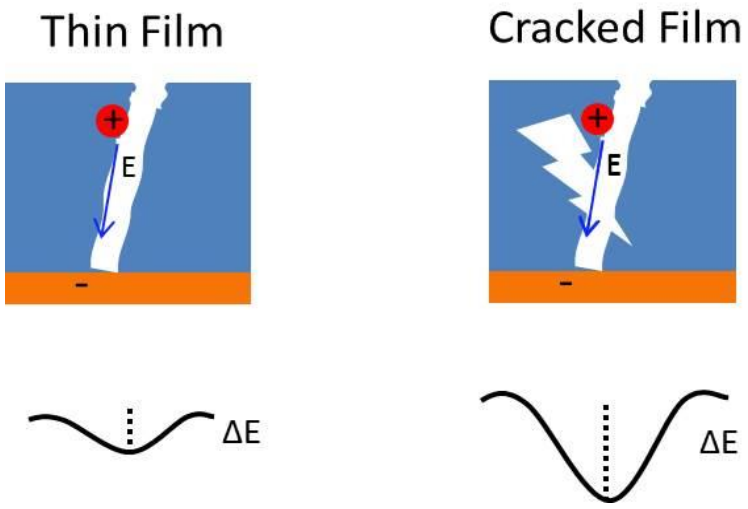

Figure 4.1.6 Schematic draw of the ion transport in the ice films along the pores. ΔE indicates the depth of the traps in the films, with the same scale for both films. Left: The ions migrate to the substrate along the walls of the pores. Right: Cracks in the films break the migration path. A fraction of the ions are trapped in the crack-induced voids, which are much deeper trapped, compared to those in the thin film on the left.

If heated at the same rate, one may notice that the temperature at which the surface potential decreases to zero over the crystallization range (160 – 190 K) is lower for the film having a larger initial porosity, as shown in Figure 4.1.5. This is unlikely due to sublimation of the films, since it is confirmed that films sublimate significantly above 190 K with the corresponding QCM frequency, the microscopic images and some cases the mass spectrometer. In addition, the film with a larger porosity is thicker and is expected to desorb at higher temperature [15]. Rather, the temperature dependence of the surface potentials of cracked films over the phase transformation range (~160 K) may be evidences supporting the possibility that porosity facilitates crystallization in the ice films.

Summary and Conclusion

An ASW film will crack spontaneously during growth above a critical thickness that increases with deposition temperature and incidence angle of the vapor flux. The geometry of cracks develops from small-scale, dense, and ramified patterns to large, sparse, and nearly-straight lines as the deposition temperature increases. When heating a film whose thickness is close to the critical thickness, more cracks are formed at temperatures much lower for the onset of phase transformation.

Dielectric depolarization occurs in ASW films during cracking, due to relaxation of local molecules caused by the released strain energy. If the cracked films are heated, the crack-induced defects trap a fraction of the aligned dipoles or the deposited charge up to elevated temperatures as high as ~100 K. The trapped dipoles / charge slowly decay

above 100 K. Surface potentials of the cracked films reduce to zero over phase transformation range (~160 K), and the temperature where the surface potential disappears depends on the initial porosity of the films, suggesting that the porosity probably facilitates crystallization in the films.

Water ice is abundant on the surfaces of many objects in the outer solar system. Most of our knowledge about the icy surfaces comes from studies of reflected solar light. It is likely that cracks result in variations of reflectance across icy surfaces, a consequence particularly important to optical remote sensing. Crack-induced defects may trap charges in the icy bodies, creating surface potentials which may deflect and even reflect magnetosphere particles from reaching the surfaces of the icy satellites and may need to be considered in astrophysical applications.

Acknowledgments

This work was supported by NASA Outer Solar System Program.

References

[1] B. Schmitt, C. De Bergh, M. Festou, *Solar System Ices*. Kluwer, Dordrecht (1998)

[2] R. A. Baragiola, *Planetary and Space Sci.* **51**, 953 – 961 (2003)

[3] R. A. Baragiola, in *Water In Confining Geometries*, edit by J. P. Devlin and V. Buch (Spring, Berlin, 2003)

[4] E. Mayer and R. Pletzer, *Nature* (London) **319**, 298 (1986)

[5] K.P. Stevenson, Greg A. Kimmel, Z. Dohnalek, R. Scott Smith, and Bruce D. Kay, *Science* **283**,1505 (1999)

[6] U. Raut, B. D. Teolis, M. J. Loeffler, R. A. Vidal, M. Fama, and R. A. Baragiola, *J. Chem. Phys.***127**, 244511 (2007)

[7] N. J. Sack, R. A. Baragiola, *Phys. Rev. B* **48**, 9973 – 9978 (1993)

[8] J. Hessinger, B. E. White Jr and R. O. Pohl, *Planet Space Sci.* **44**, 937 – 944 (1996)

[9] B. E. Wood and J. A. Roux, *J. Opt. Soc. Am.* **72**, 720 (1982)

[10] M. S. Westley, G. A. Baratta, and R. A. Baragiola, *J. Chem. Phys.* **108**, 3321 (1998)

[11] T. C. Sivakumar, S. A. Rice, and M. G. Sceats, *J. Chem. Phys.* **69**, 3468 (1978)

[12] J. A. Ghormely and C. J. Hochanadel, *Science* **171**, 62 (1971)

[13] M. A. Allodi et al., *Space Sci. Rev.* **180**, 101 (2013)

[14] C. Bu, J. Shi, and R. A. Baragiola, to publish

[15] N. J. Sack, R. A. Baragiola, *Phys. Rev. B* **48**, 9973 (1993)

[16] J. Shi, M. Fama, B.D. Teolis, R. A. Baragiola, *Phys. Rev. B* **85**, 035424 (2012)

[17] Ziegler and J. P. Biersack, SRIM 2003, Stopping and range of ions in matter, 2006 (available at www.srim.org)

[18] R. W. Hoffman, Surf. Interf. Anal. 3, **62** (1981)

[19] J. A. Floro, S. J. Hearne, J. A. Hunter, and P. Kotula, *J. Appl. Phys.* **89**, 4886 (2001)

[20] B. W. Sheldon, A. Lau, and A. Rajamani, *J. Appl. Phys.* **90**, 5097 (2001)

[21] J. A. Floro, P. G. Kotula, and S. C. Seel, *Phys. Rev. Lett.* **91**, 9 (2003)

[22] A. A. Griffith, Phil. Trans. Roy. Soc. 221 (1921) 163

[23] Z. Dohnalek, G. A. Kimmel, P. Ayotte, R. S. Smith, and B. D. Kay, *J. Chem. Phys.* **118**, 364 (2003)

[24] W. L. Brown, L. J. Lanzerotti, J. M. Poate, W. M. Augustyniak, *Phys. Rev. Lett*. **40**, 1027 – 1030 (1978)

[25] G. Strazzulla, L. Torrisi, G. Foti, *Europhys. Lett*. **7**, 431 – 434 (1988)

[26] A. A. Tsekouras, M. J. Iedema, and J. P. Cowin, *Phys. Rev. Lett.* **80**, 26, (1998)

4.2 Effects of gas desorption induced cracking on electrical properties of amorphous solid water

Abstract

We have studied the structural and electrical properties of amorphous solid water (ASW) films (1120 ML, 1 ML = 1×10^{15} molecules/cm^2) deposited on top of Xe films (710 ML) at 10 K. We observed Xe desorption and the thermally induced decay of the spontaneous polarization potential and the electrostatic potential induced by slow ion irradiation for single films and bilayer water-Xe films. Cracking was observed in ASW on Xe films at (44±1) K, and continued at temperatures from 45 K to 70 K while Xe desorbed from the water films into the vacuum. In contrast, similar bilayer films, with Xe on top showed no apparent cracks, but similar decay of the surface voltage upon heating. Measurements of surface potentials of the cracked films with annealing temperature suggested that traps at Xe-water interface and at cracks hinder the transport of charges across the condensed films at temperatures between 44 K and 140 K.

Introduction

Condensation of water vapor onto cold substrates (below ~130 K) in vacuum forms amorphous solid water (ASW), the focus of much fundamental research due to its occurrence in astronomical environments [1]. The absorption, retention and desorption of gases within ASW provide information about the structure and other properties of the ASW. Early work in this field was done by Bar-Nun *et al.* [2, 3], probing the structure

and dynamics of ASW by monitoring the trapping and release of gases by ASW. Gas adsorption experiments revealed a microporous (defined as pores with width < 2 nm) structure in the ASW with accessibility to the external surface, presenting an adsorption area as high as hundreds of m^2/g [4]. The microporosity ($p = 1 - \rho/\rho_c$, where ρ is the density of the ASW and ρ_c is the intrinsic density of the compact water ice) of ASW strongly depends on the growth conditions [4, 5] and subsequent processing, e. g., thermal annealing [4 , 6], and ion irradiation [7].

In most of these earlier studies, gas incorporation in ASW was done by exposing water ice films to a directed gas flux [2] or a background pressure of gas [6], or by co-depositing mixtures of gases and water [3]. Upon heating, gases used in these experiments were more volatile than the water ice and desorbed at low temperatures after migrating through the pore networks to reach the surface of the films [2, 3, 4, 6]. Some of the pores were closed as the temperature increased, and a fraction of the gases was trapped in the closed pores and later desorbed at about 150 K, migrating through the newly formed grain boundaries or cracks due to crystallization of the water ice [2, 3]. Recently, Kay *et al*. [8, 9] studied the desorption kinetics of a variety of volatile gases from overlayers of ASW. Their data suggested that new connected pathways were formed in the water overlayer during the nucleation and growth of crystalline ice from ASW, giving rise to the episodic release of gases at about 150 K.

Recent work by our laboratory has studied the effects of the pore networks on electrical properties of ASW [10, 11]. To further understand the relationships among the structure, gas adsorption/desorption and electrical properties of ASW at low temperatures

(<150 K), we have brought to this problem several additional experimental techniques. They include 1) vacuum microbalance for absolute measurements of desorption, 2) optical microscopy to reveal the development of surface structure, 3) electrostatic charging with low energy ions and 4) a Kelvin probe to determine the surface potentials of the films.

Experimental Details

Experiments were conducted in an ultra-high vacuum system (Figure 2.1) with a base pressure of ~2×10^{-10} Torr. ASW or Xe films were deposited onto a gold-coated quartz crystal microbalance (QCM), which was cooled by an open cycle liquid helium cooling system. The areal mass (m/A) of the deposited film was measured with the resulting change (Δf) in the frequency of the QCM:

$$\frac{m}{A} = -s \times \Delta f \tag{1}$$

where $s = 1.227 \times 10^{-8}$ g· s· cm^{-2} is Sauerbrey's constant [12]. The column density n of the film in units of monolayer (ML defined as 1×10^{15} molecules/cm^2) was derived with

$$n = -\frac{m}{A} \cdot \frac{1}{10^{15} \times M} \tag{2}$$

where M is the molecular mass. Surface potentials of the films were deduced from measurements of the contact potential difference (CPD) with a Kelvin probe (KP Technology Ltd, UHV KP 4.5), with a resolution better than 0.05 V [13]. The microstructure of the film surfaces was imaged with a long-distance microscope (Questar

QM-100) coupled to a digital camera at a working distance of 9 inches (resolution of ~3 μm).

ASW films were deposited at 10 K from high-purity water vapor flux passing through a collimating micro-capillary array doser [14] at the incidence angle of 45°. Column densities of the ASW films were 1120 ML, measured with the QCM; thicknesses of the ASW films at growth temperature (10 K) were (540±17) nm, obtained from optical interference measurements [15]. Densities of the ASW films at 10 K were $\rho_{H_2O} = (0.62 \pm 0.02)$ g ·cm^{-3}, calculated from the ratios of the column densities to the film thicknesses. Xe films were either deposited at 40 K from a collimated gas flux passed through the same doser at normal incidence, annealed to 60 K, and then cooled to 10 K, or deposited at 10 K on top of an ASW layer. Column densities of the Xe films were 710 ML; the thicknesses of the Xe films were ~450 nm, calculated from the ratios of the measured column densities to the given densities of $\rho_{Xe} = 3.44$ g ·cm^{-3} at temperatures below 60 K [16]. The gas manifold used for deposition was pumped for 2.5 hours to a pressure of ~20 mTorr when switching the depositing vapor/gas. The purity of the gas/vapor was routinely verified with a quadrupole mass spectrometer (QMS) (Stanford Research Systems, RGA 100) with m/z = 18 (H_2O^+ ions) for water signal and m/z = 66 (Xe^{++} ions) for Xe, where m/z is the ratio of mass to charge.

Three types of films were prepared: (I) ASW films (1120 ML), (II) Xe films (710 ML), and (III) double-layer films consisting of 710 ML Xe with 1120 ML ASW on top. The layer order of the double-layer films (Type III) was switched in some experiments. Unless specified, the double-layer films refer to type III films with ASW films on top of

Xe films. Another set of films were prepared with identical procedures as (I, II, III), and irradiated with low energy ions (500 eV He+) at normal incidence for 270 seconds to a fluence of $(0.9 \pm 0.1)\times10^{12}$ cm^{-2} s^{-1}. The ions were produced by a low energy ion gun (Nonsequitur Technologies, M1401, E = 0.005 – 5 keV). The flux was measured by a Faraday cup and was kept at $(0.33 \pm 0.04) \times 10^{10}$ cm^{-2} s^{-1}. All of these films were rotated to face the Kelvin probe to measure the surface potentials while heating from 10 K to 200 K at a rate of 1.8 K/min. The surface microscopic structure of the films was examined by the microscope aimed at 45° relative to the Kelvin probe. Temperature programmed desorption (TPD) spectra were obtained with the QMS. The total mass loss due to desorption could also be derived from the change in the frequency of the QCM. We show cracks, structural failures in the ASW films resulting from desorption of the underlying Xe films as the temperature increases, followed by the effects of the cracks on the electrical properties of the water overlayers.

Results and discussions

A. Desorption induced cracking in the ASW films

A.1. Single ASW and Xe films

QCM measurements (Figure 4.2.1) show that, for our film thickness and heating rate, the desorption temperatures are 176 ± 2 K for ASW films and 68 ± 2 K for Xe films. The microscope shows no cracks in these single-layer films, neither at the growth temperature nor during annealing.

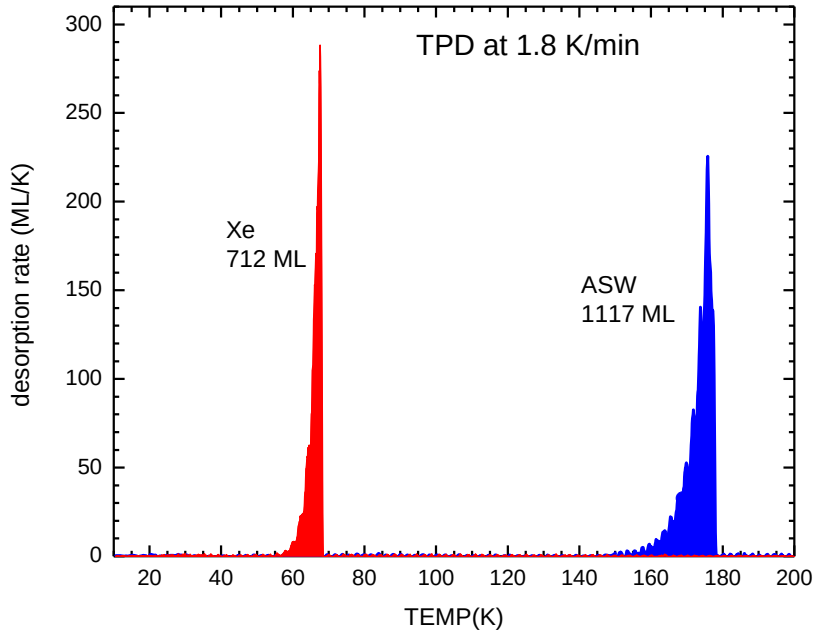

Figure 4.2.1 Desorption peaks from single-layer ASW and Xe films from the QCM measurements.

A.2. Double-layer films

When heated, the double-layer films with ASW films deposited on top of Xe films behaved dramatically different as shown in the following.

TPD spectra (Figure 4.2.2) for the double-layer film without deposited charges show that Xe desorbs in four different temperature ranges: 49 – 74 K, ~151 K, ~166 K and ~174 K (peaks 1 – 4 in the left panel of Figure 4.2.2). These desorption peaks are consistent with those found in experiments with water films subjected to flowing gas [2] or with co-deposits of mixtures of gases and water [3]. To understand this behavior, we

recall that water ice condensed at 10 K with 45° incidence is nanoporous [5]. Since most of the pore networks are connected to the exterior surface of the water ice [4, 5, 6], gas from the underlying Xe film can enter into the water ice, migrate through the water ice and desorb from the surface of the water ice. The pore structure collapses simultaneously as the temperature increases [4, 6], and Xe atoms, if unable to desorb through the water ice at low temperatures at 40 - 74 K, are trapped inside the water ice in the closed pores. At ~151 K, crystallization of the water ice produces grain boundaries and cracks which are easy paths for Xe desorption [8, 15], resulting in the desorption peak of Xe [2, 15]. The phase transformation from cubic ice to hexagonal ice around ~166 K releases additional Xe [2]. A fraction of the Xe is unable to desorb in the first three ranges, perhaps by being trapped at the film/gold interface, and is finally released when the whole water ice film evaporates at a desorption temperature of ~174 K [2].

The double-layer films (without/with deposited charges) fracture at (44±1) K, indicated by the sudden appearance of cracks in the microscope as shown in Figure 4.2.3. The cracks evolve as the temperature raises from 44 K to ~74 K during desorption of the Xe gases and stabilizes above ~80 K. When the films are heated over the crystallization temperature range around 150 K, additional cracks appear, associated with additional Xe desorption shown in Figure 4.2.2. The cracking doesn't appear to be a function of deposited surface charge, and the pattern of the cracks is random and irreproducible. The cracking of the double-layer films is accompanied with an abrupt shift in the frequency of the QCM at (44±1) K. Since the frequency of the QCM is sensitive to stress [12, 17], the abrupt shift in the QCM frequency indicates stress relaxation in the double-layer films.

In another experiment, we switched the order of the double-layer film by directly depositing the Xe film on top of the ASW film at 10 K, and didn't observe any cracks or sudden shift in the QCM frequency during heating, which suggests that the desorption of Xe atoms underneath the ASW film is the prerequisite of the formation of cracks.

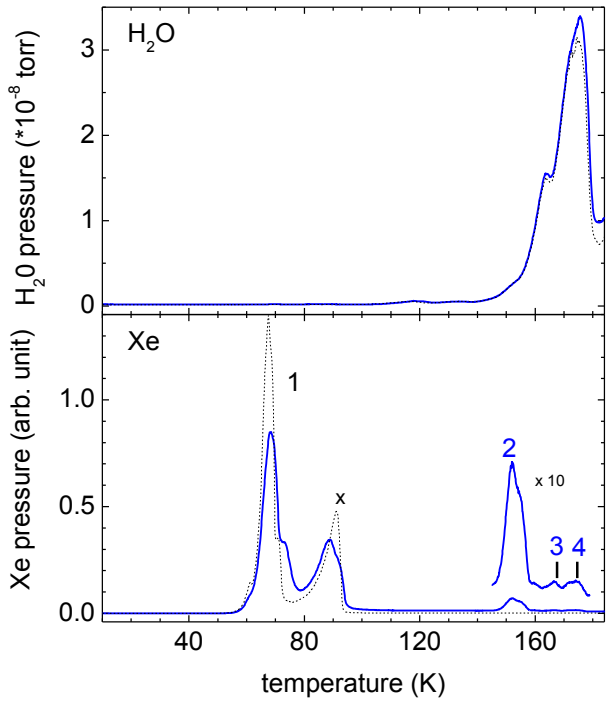

Figure 4.2.2 TPD spectra of films grown at 10 K and heated at 1.8 K/min. The thickness for the ASW films was 1120 ML, and was 710 ML for the Xe films. Solid-line, an ASW film deposited on a Xe film; dashed-line, a pure ASW film (top panel), and a pure Xe film (bottom panel). Peak x is a spurious peak due to desorption of gas from other parts of the sample stage.

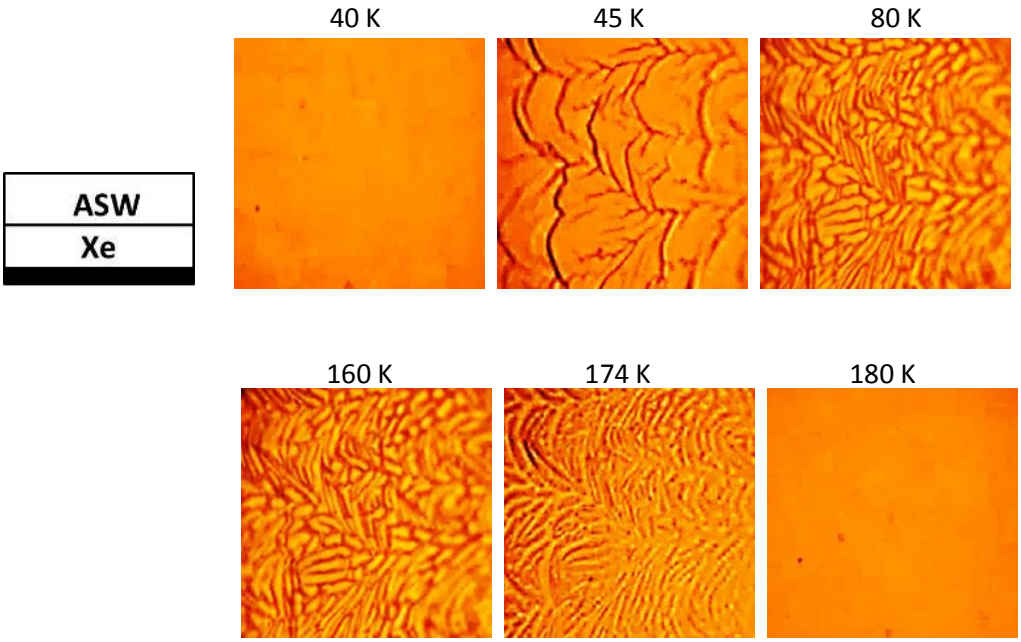

Figure 4.2.3 Evolutions of cracks with annealing temperature in the double-layer films: 1120 ML ASW layer atop a 710 ML Xe layer. The field of view is 700 μm ×700 μm.

B. Effects of cracks on electrical properties of the ASW films

Recent work by our laboratory shows that the microporosity of ASW affects the spontaneous polarization and transport of ions in ASW films [10, 11]. In this paper, we studied effects of the desorption-induced cracks on the electrical properties of water ice by measuring the surface potentials of the films. We present the results about the spontaneous polarization and electrostatic charging of the double-layer films at 10 K, followed by the evolution of the surface potentials with temperature when the films are heated from 10 K to 200 K.

B.1. initial surface potential

ASW films condensed onto cold substrates (<110 K) develop a spontaneous polarization due to partial alignment of the water molecules during growth and manifested as a negative surface potential [18]. The surface potentials of the 1120 ML ASW films deposited at 10 K at 45° incidence atop the QCM or preexisting Xe layers were $-(17.3\pm 0.3)$ V. The surface potentials of the Xe films (710 ML) were $-(0.09\pm 0.05)$ V and didn't change with temperature between 10 K and 60 K. Xe atoms are non-polar atoms, and we attribute the observed small voltages in the Xe films to the change in work function of the substrate, the gold electrode of the QCM. In some experiments, we deposited a 710 ML Xe film on top of a 1120 ML ASW film at 10 K, and the surface potential changed from $-(17.3\pm 0.3)$ V to $-(16.4\pm 0.3)$ V after adding the Xe overlayer.

B.2. Electrostatic charging at 30 K

With a charge Q deposited on top of a dielectric film (of thickness d) on an electrically grounded metal substrate, a voltage (V) is created across the film:

$$V = \frac{Qd}{A\varepsilon_o\varepsilon} \tag{3}$$

where A is the irradiated area, ε_o is the permittivity of vacuum, and ε is the dielectric constant of the film. For a double-layer system, Eq. (3) is modified as

$$V = \frac{Q}{A\varepsilon_o}.\left(\frac{d_1}{\varepsilon_1} + \frac{d_2}{\varepsilon_2}\right) \tag{4}$$

where the subscript refers to the layer number.

The established value of the dielectric constant of dense ice is ε_{H_2O} = 3.2 [19], and ε_{Xe} = 2.0 for Xe [16]. At the reduced density of the ASW film in our experiment, the dielectric constant is 2.2, according to the Clausius-Mossotti equation, $\frac{\varepsilon-1}{\varepsilon+2} = K\rho$ (where Kdepends on the molecule and temperature) that relates the dielectric constant to the density ρ. If there is a strong leakage of the deposited charges to the substrate during irradiation, then the observed voltage would require that the calculated value of ε_{H_2O} or ε_{Xe} based on Eq. (3) and Eq. (4) be much larger than their established values. If the water dipoles immediately respond to the ion-induced electric field, the calculated value of ε_{H_2O} will also be significantly larger from the electronic value appropriate at low temperatures.

The thickness of the Xe layer is about 450 nm, and the surface potential of the Xe film increases from −(0.09±0.05) V to +(1.8±0.1) V when irradiated with the same fluence as the ASW film. The calculated ε_{Xe} at 10 K based on Eq. (3) is (41±8), much

larger than its established value of 2.0. We explain this disagreement by the leakage of the deposited charges through the Xe film to the substrate, since the extrapolation of the hole mobility in solid Xe at 10 K is as high as 1.5 $cm^{-2}s^{-1}V^{-1}$ [20]. The small surface voltage (~1.8 V) results from charges trapped at defects or impurities in the Xe film [21].

The surface potential of the double-layer film changes from −(17.2±0.3) V to +(56.2±0.5) V when irradiated with the same fluence as the ASW films. Therefore, the calculated ε_{H_2O} at 10 K is 2.1 based on Eq. (4), given ε_{Xe} = 2, d_{Xe}= 450 nm, and d_{H_2O}= 540 nm. This calculated ε_{H_2O} agrees with the value 2.2 given above, based on the Clausius-Mossotti equation, suggesting that most of the deposited charges stay near the external surface of the ASW layer. In one experiment, we switched the order of the doubly-layer film by deposited the Xe layer atop the ASW layer, and then irradiated this double-layer film to the same fluence as above, the surface potential changed from −(16.4±0.3) V to +(33.5±0.5) V. This surface potential of +33.5 V is much smaller than +56.2 V (for double-layer film with ASW on top) but larger than +21.8 V (for single-layer ASW film), which suggests most of the deposited charges have migrated, as expected, through the Xe to the interface of the two layers during irradiation where a fraction were trapped, as will be discussed below.

B.3. Evolution of the surface potentials during heating

While heating, no cracks were observed in the single-layer ASW films or the double-layer films with Xe layer atop ASW layer. However, the double-layer films with ASW layer atop the Xe layer fractured at temperatures above 44 K. We focus on the

crack-induced evolutions of surface potentials as a function of heating temperature from 10 K to 200 K in the following.

The evolutions of surface potentials of the films without / with deposited charge are shown in Figure 4.2.4 (a and b). At temperatures below 44 K, where no cracking occurs, surface potentials of the double-layer films behave similarly as those of the single layer water films. However, above 44 K, the surface potentials of the double-layer films show new features induced by the cracks.

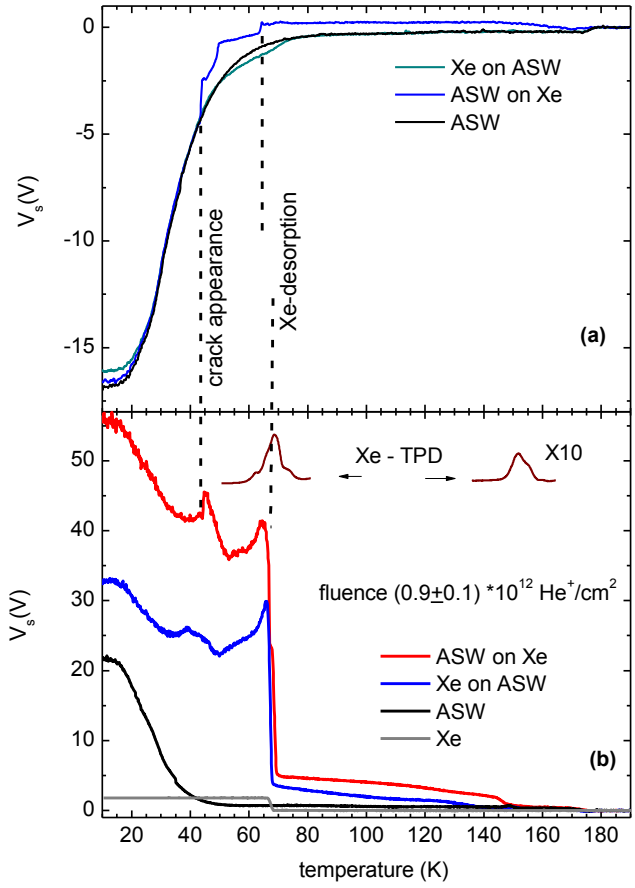

Figure 4.2.4 Surface potential *vs.* annealing temperature. All the ASW films were deposited at 10 K at 45° incidence, with column densities of 1120ML. The Xe layers were deposited at 40 K at normal incidence, heated to 60 K and then cooled to 10 K; except for the cases that Xe was deposited on top of ASW, where Xe was deposited at 10 K at normal incidence. Column densities of the Xe layers were 710 ML. The TPD spectrum of the Xe was for the irradiated double-layer film with ASW atop Xe (red line in b). The heating rate was 1.8 K/minute.

The thickness of the double-layer films changes from (540 + 450) nm to ~ 540 nm at about 70 K where most of the Xe atoms desorb from the water layer (on top or underneath), ignoring the small vertical compaction of the films during heating due to the collapse of pores in microporous ASW. The drop in thickness at ~70 K causes the large decrease in surface potentials of the double layer films (Figure 4.2.4a & 4b). In contrast to the single-layer water or Xe films, the retained surface potentials at temperatures above 70 K in the irradiated double-layer films are much larger, regardless of the layer order. This indicates that a fraction of the deposited charges are trapped in the crack-induced defects (ASW film atop Xe film) or immobile Xe+H_2O traps. These trapped charges decay slowly as temperature increases; the leakage of the trapped charges to the substrate is facilitated by crystallization of the ASW films, resulting in a sharp decrease in the surface potentials at about 150 K.

We now turn our attention to the sharp features, for which we attempt a qualitative discussion since the exact location of the charges in unknown.

In Figure 4.2.4, the surface potentials of the cracked double-layer films show abrupt positive shifts at the onset of cracking at 44 K. It is likely that the energy released during cracking results in a rise of the local temperature thereby a local depolarization and/or crystallization in the water films. A rise in surface potentials of irradiated water films over the crystallization range at ~150 K was observed in an earlier study [22], consistent with this proposed crystallization during cracking at about 44 K.

The decrease of the voltage of the two double-layer water-Xe films show a behavior typical of the pure ASW films, attributed to leakage through the pore structure, plus some sharp features in the range 45 – 65 K. Since charge leaks near completely below 44 K in pure ASW films, we attribute this behavior to trapping sites. They can be at cracks (but the slower discharging also occurs through the Xe on water films, which are not seen to crack) and at the interface between water and Xe. The diffusion of Xe onto the microporous ASW starts near the onset of cracking and leads both to the increase of ε_{ASW} and the decrease of ε_{Xe}. The net effect in the voltage (Eq. 4) is uncertain but we note that an increase in voltage would result if the decrease in ε_{Xe} is dominant . We propose that the first increase, near 45 K, is due to Xe diffusing inside the pores of ASW until they are full (we notice in Figure 4.2.2 that there is no significant desorption of Xe at this temperature). This process decreases the dielectric constant of Xe and increases that of the porous ASW. At about 62 K, Xe starts to desorb (Figure 4.2.2) and is nearly depleted after a few degrees. The fact that the voltage of both double layer films: Xe on ASW and ASW on Xe, drop drastically at this temperature suggests that the trapped charge above 44 K was at the interface between the films. The interface traps may be in the form of Xe–$(H_2O)_n$ complexes, bound by the polarization of water clusters induced by the Xe^+ charge.

Summary and Conclusion

ASW films were deposited on top of Xe layers at 10 K at 45° incidence and then heated to 200 K at a rate of 1.8 K/minute. Upon heating, microscopic images of the surfaces showed that cracks appear at (44±1) K and continue to evolve until about 74 K,

due to Xe desorption through the water ice overlayer. Crystallization of the ASW films at about 150 K results in more cracks, associated with additional Xe desorption. A fraction of Xe remains trapped and desorbs when the water ice films evaporate at about 174 K. Surface potentials of the double-layer films shows that the spontaneous polarization and dielectric constant of ASW films at 10 K is independent of the underlying Xe layers. Upon heating, the crack-induced grain boundaries / defects hinder the transport of the ions through the water films to the substrate, and the leakage of the trapped ions is enhanced during crystallization of the water films at about 150 K.

The results may have implications for the ubiquitous ASW in the outer solar system and interstellar grains. Studies here show that cracks trap the charges in the water ice, creating a surface potential. Inhomogeneous surface electric fields may deflect and even reflect particles with the same polarity from reaching the surfaces of the icy bodies and would need to be considered when studying plasma-surface interactions.

References

[1] R. A. Baragiola, in *Water In Confining Geometries*, edited by J. P. Devlin and V. Buch (Springer, Berlin, 2003)

[2] Bar-Nun, G. Herman, and D. Laufer, *Icarus* **63**, 317-332 (1985)

[3] Bar-Nun, J. Dror, E. Kochavi and D. Laufer , *Phys. Rev. B* **35**, 5 (1987)

[4] E. Mayer and R. Pletzer, *Nature* (London) **319**, 298 (1986)

[5] K.P. Stevenson, Greg A. Kimmel, Z. Dohnalek, R. Scott Smith, and Bruce D. Kay, *Science* **283**,1505 (1999)

[6] U. Raut, M. Fama, B. D. Teolis, and R. A. Baragiola, *J. Chem. Phys.* **127**,244511 (2007)

[7] U. Raut, B. D. Teolis, M. J. Loeffler,R. A. Vidal, M. Fama, and R. A. Baragiola, *J. Chem. Phys.* **126**, 244511 (2007)

[8] R. S. Smith, C. Huang, E. K. L. Wong, and B. D. Kay, *Phys. Rev. Lett.* **79**, 909 (1997)

[9] R. May, R. Smith, and B. Kay, *J. Chem. Phys.* **138**, 104502 (2013)

[10] C. Bu, J. Shi, and R. A. Baragiola, to be published

[11] C .Bu and R. A. Baragiola, to be published

[12] M. A. Allodi et al., *Space Sci. Rev.* **180**, 101 (2013)

[13] J. Shi, M. Fama, B.D. Teolis, R. A. Baragiola, *Phys. Rev. B* **85**, 035424 (2012)

[14] N. J. Sack, R. A. Baragiola, *Phys. Rev. B* **48**, 9973 (1993)

[15] M. S. Westley, G. A. Baratta and R. A. Baragiola, *J. Chem. Phys.* **108**, 8 (1998)

[16] R. l. Amey and R. H. Cole, *J. Chem. Phys.* **40**, 146 (1964)

[17] E. P. Eernisse, *Applications of Piezoelectric Quartz Crystal Microbalances* (Elsevier, Amsterdam, 1984), chap. 4; E. P. Eernisse, *J. Appl. Phys.* **43** (1972) 1330

[18] M.J. Iadema, M.J. Dresser, D. L. Doering, J. B. Rowland, W.P. Hess, A. A. Teskouras, and J. P. Cowin, *J. Phys. Chem. B* **102**, 9203 (1998)

[19] P. V. Hobbs, Ice physics (Clarendon, Oxford, 1974)

[20] W. Ehrenberg and D. J. Gibbons, electron bombardment induced conductivity and its application, Academic Press, London (1981)

[21] R. A. Baragiola, M. Shi, R. A. Vidal, and C. A. Dukes, *Phys. Rev. B*, **58** 19 (1998)

[22] A. A. Tsekouras, M. J. Iedema, and J. P. Cowin, *Phys. Rev. Lett.* **80**, 26, (1998)

Chapter Five

Conclusion

We deposited ASW films on cold substrates from a collimated vapor flux passed through a micro-capillary doser. We used quartz crystal microgravimetry and ultraviolet-visible spectroscopy to characterize the porosity of the films. The microstructure of the surfaces of the films was visually characterized by a long-distance microscope coupled with a digital camera. The degree of spontaneous polarization was interpreted from measurements of the contact potential difference with a Kelvin probe. We also charged the surfaces of the ASW films by irradiation with low-energy ions (500 eV) to study the electrostatic charging/discharging with a Kelvin probe. The main conclusion of this work is that the polarization and motion of ions in ASW at low temperatures strongly depend on the pores and cracks.

An ASW film shows a negative surface potential if grown at temperatures below 110 K by vapor deposition because of partial alignment of the water molecules during condensation. This negative surface potential increases linearly with film thickness at a slope that decreases with deposition temperature. The surface potential decreases with incidence angle of the vapor flux. When the film is heated, its surface potential decreases irreversibly by 80% at a temperature ~30 K above the deposition temperature. The surface potential also decreases with time if the film is held at a constant annealing temperature. Our data show that the polarization is governed by the relaxation of the micropore structure rather than changes in intrinsic dielectric behavior of the water

network. We propose that the observed surface potential results from a fraction of aligned water dipoles (~9% if deposited at 30 K at normal incidence) on the internal surface of the pores with the oxygen lone pair electrons preferentially pointing towards the external surface. Within this picture, depolarization, and thereby a decrease in the surface potential, occurs during the collapse of the pores. If a film cracks, induced by intrinsic tensile stresses during growth above a critical thickness or by desorption of the subjacent volatile gases upon heating, depolarization occurs, reducing its surface potential. However, when the cracked film is heated, the crack-induced defects retain the molecular alignment to elevated temperatures (above 100 K).

An ASW film has a dielectric constant of (3±0.5) at 30 – 100 K. When an irradiated ASW film is heated, its surface potential irreversibly decreases, and the sharp decreases of the surface potential at a temperature somewhat higher than the pre-annealing temperature is interpreted as a leakage of charge to the substrate. We found that the evolution of the surface potential with temperature/time strongly depends on the microstructure of the pores in the film. We suggest that the thermal-induced rearrangement of the water molecules on the walls of the pores facilitates the motion of the deposited charges to the metal substrate. Experiments with the cracked films showed that the crack-induced defects trap a fraction of the deposited charges to elevated temperatures up to ~100 K.

The findings in this thesis provide new explanations for the observations in the studies on the electrical properties of ASW, by taking the microstructure of the pores or cracks into account. Water ice is abundant on the surfaces of many objects in the outer

solar system. This work will help enhance understanding of ice structure, ice-ion interactions and other charge-related processes in the Outer Solar System. Effects of microstructure on the electrical properties of ASW films presented in this thesis provide more relevance to modelers to refine their parameters when modeling the icy surfaces in space.

There are still some open questions. Upon heating, the evolutions of the surface potentials, induced by the polarization or deposited charges, depend on the porosity of the films; however, the decrease in the porosity is much slower than that in the surface potential. Infrared spectra of water ice taken in other studies suggest that thermal annealing reduces the surface areas of the pores more effectively than the volume of the pores. Laboratory characterization of the distribution of the aligned dipoles in the film during condensation and the evolution of the alignment during irradiation or annealing are still missing. More convincing evidence supporting the conclusions in this work should include simultaneous characterization of the pore structure and configuration of the water molecules on the internal surface area with other experimental techniques, e.g., infrared absorption spectrometry and positron beam spectroscopy.

We observed that an ASW film spontaneously cracks during growth above a threshold thickness that increases with deposition temperature and incidence angle of the vapor flux. However, the mechanism for cracking is not fully understood yet. Future work may include the quantitative measurement of stresses in the film during growth. One proposed method is to deposit the water ice films on a cantilever that functions at low temperatures. The stress in the film during condensation can be derived from in situ

measurements of the cantilever curvature using a multi-beam optical stress sensor. Measurements of surface potentials suggest that cracks trap the intrinsic aligned dipoles and deposited charges to temperatures as high as 100 K; however, trapping mechanism is poorly understood. Most of our knowledge about the icy surfaces comes from studies of reflected solar light. It is likely that cracks result in variations of reflectance of low-temperature ices, which is of particular importance to optical remote sensing. The cracks may also create surface potentials which may deflect and even reflect magnetosphere particles from reaching the surfaces of the icy satellites. A deeper understanding of cracking in the water ice may be helpful in astrophysical applications.